

# CORRELATION BETWEEN GALAXY MERGERS AND LUMINOUS ACTIVE GALACTIC NUCLEI

Jueun Hong<sup>1,2,6</sup>, Myungshin Im<sup>1,6</sup>, Minjin Kim<sup>3</sup>, & Luis C. Ho<sup>4,5</sup>

<sup>1</sup>*Center for the Exploration of the Origin of the Universe (CEOU), Astronomy Program,  
Department of Physics & Astronomy, Seoul National University, Seoul, Republic of Korea*

<sup>2</sup>*Donga Science Co., Ltd., 7th Floor, 109, Cheongpa-ro, Yongsan-gu, Seoul, 140-877, Korea*

<sup>3</sup>*Korea Astronomy and Space Science Institute, Daejeon 305-348, Korea*

<sup>4</sup>*Kavli Institute for Astronomy and Astrophysics, Peking University, Beijing 100871, China*

<sup>5</sup>*The Observatories of the Carnegie Institution for Science, 813 Santa Barbara Street,  
Pasadena, CA 91101, USA*

<sup>6</sup>jueunhong@astro.snu.ac.kr, mim@astro.snu.ac.kr

## ABSTRACT

It is not yet clear what triggers the activity of active galactic nuclei (AGNs), but galaxy merging has been suspected to be one of the main mechanisms fuelling the activity. Using deep optical images taken at various ground-based telescopes, we investigate the fraction of galaxy mergers in 39 luminous AGNs ( $M_R \lesssim -22.6$  mag) at  $z \leq 0.3$  (a median redshift of 0.155), of which the host galaxies are generally considered as early-type galaxies. Through visual inspection of the images, we find that 17 of 39 AGN host galaxies (43.6%) show the evidence for current or past mergers like tidal tails, shells, and disturbed morphology. In order to see if this fraction is abnormally high, we also examined the merging fraction of normal early-type galaxies in the Sloan Digital Sky Survey (SDSS) Strip 82 data (a median redshift of 0.04), of which the surface-brightness limit is comparable to our imaging data. To correct for the effects related to the redshift difference of the two samples, we performed an image simulation by putting a bright point source as an artificial AGN in the images of SDSS early-type galaxies and placing them onto the redshifts of AGNs. The merging fraction in this realistic sample of simulated AGNs is only  $\sim 5 - 15\%$  (1/4 to 1/8 of that of real AGNs). Our result strongly suggests that luminous AGN activity is associated with galaxy merging.

*Subject headings:* galaxies: active — galaxies: nuclei — galaxies: general — galaxies: evolution — galaxies: interaction — galaxies: quasars

## 1. INTRODUCTION

An active galactic nucleus (AGN) is an energetic core of a galaxy whose energy comes from accretion of surrounding matter by a supermassive black hole (SMBH) that resides at the central part of the galaxy. In order for an SMBH to shine as an AGN, it needs a supply of gas to fuel its activity. Two main mechanisms have been suggested to trigger AGN activity: an internal mechanism through a dynamical instability inside a galaxy and an external mechanism through galaxy-galaxy interaction or merging. However, it is not yet clear which one is the dominant mechanism, even after many observational studies have been carried out.

The internal mechanism is such that a gas inflow to the central part occurs as a result of instability in the internal structure of a galaxy. For example, a galaxy bar can move gas from the outer regions of a galaxy into its center, and then the gas inflow can trigger the AGN phase

(Lynden-Bell 1979; Sellwood 1981; van Albada & Roberts 1981; Combes & Gerin 1985; Pfenniger & Friedli 1991; Heller & Shlosman 1994; Bournaud & Combes 2002; Athanassoula 2003; Sakamoto et al. 1999). Studies of AGNs with moderate X-ray luminosity, especially the studies targeting distant AGNs, find that most of the AGN hosts are disk galaxies and do not show evidence of a major merger, supporting the idea that an internal mechanism triggers the AGN activity and the SMBH growth (Schawinski et al. 2012, 2011; Cisternas et al. 2011; Kocevski et al. 2012; Simmons et al. 2012). In the local universe, the fraction of Seyfert galaxies is found to be high in barred galaxies in the Sloan Digital Sky Survey (SDSS) data, suggesting a close connection between bar and AGN activity (Oh et al. 2012), but studies exist that point to an opposite conclusion (Lee et al. 2012).

In contrary, the external mechanism is represented by galaxy interaction or merging. In such a mechanism, gas infall during a major merging triggers AGN activity (e.g., Barnes & Hernquist 1991; Mihos & Hernquist 1996; Hopkins et al. 2005; Springel et al. 2005). There are a number of observational results that support this idea. Studies of galaxy pairs or galaxies in interaction find that the AGN fraction increases in such systems. (Ellison et al. 2011; Silverman et al. 2011; Bessiere et al. 2012). Ultraluminous infrared galaxies (ULIRGs) are suggested to harbor AGNs, and many ULIRGs are merging systems (e.g., Sanders et al. 1988a; 1988b). Binary SMBHs in some AGNs demonstrate that two or more SMBHs can merge into one SMBH (Koss et al. 2011; Komossa 2003). After all, many AGN host galaxies are found to be elliptical galaxies, which do not possess bars or disk instabilities.

One promising way to investigate the AGN and merger connection is to study objects with merging features. When two galaxies with comparable mass merge, the merging pro-

duces an early-type galaxy (Toomre & Toomre 1972; Barnes & Hernquist 1992), leaving a trace of the past merging activity in the form of tidal tails, shells, and dust lanes (Quinn 1984; Hernquist & Spergel 1992; Feldmann et al. 2008). In support of this theoretical expectation, very deep imaging of early-type galaxies find merging features in many cases (15% – 80%, depending on the depth of the image; van Dokkum 2005; Tal et al. 2009; Kaviraj 2010; Kim et al. 2012; Sheen et al. 2012). The tidal features remain for about 1-2 Gyr after the merging (Feldmann et al. 2008), which overlaps with the period of AGN activity that occurs in some models at the same timescale of roughly 1 Gyr after the merging (Hopkins et al. 2005). Therefore, if major merging triggers AGN activity, we expect the following to be seen: (1) the AGN host will be an early-type galaxy or a bulge-dominated system, (2) merging features such as tidal tails and shells should be observable preferentially in AGNs than in nonactive early-type galaxies, and (3) AGNs should be found more in spheroidal postmergers (1-2 Gyr after the merging) than in merging systems at a very early stage.

Interestingly, previous searches for merging features in AGN host galaxies have seen mixed results. Bennert et al. (2008) found that four out of five low-redshift QSO hosts show obvious merging features from deep Hubble Space Telescope (HST) imaging data. A more extensive sample of 69 QSO hosts ( $0.142 \leq z \leq 0.198$ ) was imaged by a ground-based telescope, and it was found that 60% of the sample shows signs of interaction (Letawe et al. 2010). Koss et al. (2011) studied the fraction of mergers in the Swift BAT-selected AGNs and found that the fraction of BAT AGNs showing evidence of merger is much higher than the fraction in a sample of inactive galaxies (18% versus 1%). For a special class of dust-reddened AGNs, Urrutia et al. (2008) also found a high fraction of AGN hosts with evidence for ongoing or recent interaction (85%). Ramos Almeida et al. (2012) investigated the brightness of merging features in radio galaxies at  $0.05 < z < 0.7$  and found that the merging features of radio-loud active galaxies are 2 mag brighter than those of quiescent galaxies. Carpineti et al. (2012) found that about 70% of spheroidal postmergers —spheroidal galaxies with merging features—are Seyferts or LINERs. By comparing this fraction to ongoing merging systems, they suggested that the AGN phase becomes more dominant only in the very final stage of the merging. On the other hand, an early study of Bahcall et al. (1997) found that only 15% of AGN hosts show a clear indication of interaction, although they also noted a large fraction AGN hosts with close, projected companions. However, the more recent studies of Karouzos et al. (2014a, 2014b) show that there is no enhancement of close neighbors around X-ray or radio-selected AGNs with respect to field galaxies with properties similar to the AGN hosts. The aforementioned studies supporting the internal AGN triggering mechanism all find that the fractions of both early-type host galaxies and merging systems are low in distant AGNs.

These pieces of seemingly contradictory results can be resolved if AGN activities are

triggered by different mechanisms at different levels. There are theoretical studies that suggest such an idea, with the external mechanism preferentially triggering luminous AGN activity (Hopkins & Hernquist 2009; Draper & Ballantyne 2012). From an observational point of view, the studies favoring the merging mechanism are mostly based on QSOs (bright AGNs) and early-type host galaxies. In comparison, the observational studies favoring the internal mechanism are focused more on less-luminous AGNs or late-type host galaxies. Treister et al. (2012) suggest that the fraction of merging systems in AGNs is a strong function of AGN luminosity, with merging activity being stronger in more luminous AGNs (AGNs with a large bolometric luminosity). Their sample, however, is rather heterogeneous, making it difficult to draw a firm conclusion on this issue. Furthermore, a more recent study excludes a strong connection between AGNs and mergers over a wide range of X-ray luminosity ( $10^{41} < L(\text{X-ray})\text{erg}^{-1}\text{sec}^{-1} < 10^{44.5}$ ), based on their investigation of AGN host galaxies at  $0 < z < 3$  in the Chandra Deep Field south, including a careful treatment of a control sample that is compared against the morphology of the AGN host galaxies (Villforth et al. 2013). A similar conclusion was reached by Georgakakis et al. (2009) too.

Although researchers do not yet agree on the significance of merging for AGN triggering activity, it is known that host galaxies of luminous AGNs are predominantly early-type galaxies (McLure et al. 1999; Dunlop et al. 2003), i.e., products of major merging, so it is natural to consider merging as a key AGN triggering mechanism in luminous AGNs. The definition of “luminous” is a bit ambiguous, but the luminosity cut around  $M_R \sim -23\text{mag}$  qualifies as “luminous” for the central point source. While previous studies have investigated the connection between merging features and early-type hosts, the studies are rather limited in sample size (e.g., Bennert et al. 2008) or they include a heterogeneous sample of host galaxy types and are not geared to detect the faintest features (e.g., Georgakakis et al. 2009; Cisternas et al. 2011; Schawinski et al. 2011; Kocevski et al. 2012; Treister et al. 2012). While deriving the fraction of merging signatures in AGNs can be useful, interpreting the result as a sign of merger-triggered AGN activity needs an additional step of comparison with an ordinary galaxy sample because many normal early-type galaxies are found to have merging features. However, such a comparison is a complicated process because the surface-brightness limits often differ between an AGN sample and a normal galaxy sample, and the bright point sources in AGNs can make it more challenging to detect merging features.

In order to address the specific question of whether luminous AGNs are triggered by merging activity, we study the fraction of luminous AGNs showing merging features and compare it to the fraction of normal galaxies with merging features. Because the light from luminous AGNs can contaminate the outer regions of their host galaxies, deep images of luminous AGN are obtained to reveal merging features. For a similar reason, we use a control sample of normal early-type galaxies selected from the SDSS Stripe 82 data, which

reaches a surface-brightness limit of  $\mu_r \sim 27$  mag arcsec<sup>-2</sup> over a  $1'' \times 1''$  area at rms noise of  $1\sigma$  of the background regions of the image<sup>1</sup>. In addition, merging features are more difficult to find in AGN hosts than in the galaxies in the control sample because of the redshift differences and the contamination from the central point sources. Therefore, we simulated images of luminous AGNs using galaxy images in the control sample so that the simulated AGNs contain a bright central point source and are placed at redshifts similar to those of our AGN sample. This enables us to do a realistic comparison between the control sample and the AGN sample. Finally, we compare the simulated AGNs versus the real AGNs, showing that merging features are much more easily found in host galaxies of luminous AGNs than in the simulated AGNs. Throughout the paper, we adopt a concordance cosmological parameters of  $H_0 = 70$  km s<sup>-1</sup> Mpc,  $\Omega_m = 0.3$ , and  $\Omega_\Lambda = 0.7$  (e.g., Im et al. 1997). The physical quantities taken from the literature were converted to match these cosmological parameters.

## 2. AGN SAMPLE AND OBSERVATION

### 2.1. Sample Selection of AGNs

We constructed two samples of luminous type-1 AGNs at  $z < 0.3$ , one that we call as the “base sample” and another that we call as the “best sample,” which is a subsample of the base sample. The redshift cut of  $z < 0.3$  is imposed because the features that we use to trace the merging activity are overmatched by the bright point source of the AGN or become too faint to detect if a galaxy is too far away. The definitions of “luminous” are different for the two samples, and they are explained in the following.

The base sample comprises 39 luminous type-1 AGNs at  $z < 0.3$ . Here, the term “luminous” is defined to be  $M_R \leq -22.6$  mag ( $M_B < -22.0$  mag, or equivalently  $M_R < -22.6$  mag assuming B-R = 0.6), and “type-1” AGNs are selected because they have an unambiguous spectroscopic signature (broad emission lines) for the existence of an AGN. The objects are chosen with this luminosity cut without separating the nuclear component from the host galaxy light, although we gave a preference to AGNs with bright nuclear components, such as Palomar Green (PG) quasars, during the sample selection process in order to select AGNs that are luminous in the nuclear component. Our analysis will focus on the base sample because the result from the best sample does not differ much from the result from the base sample, and the base sample provides better number statistics than does the

---

<sup>1</sup>We will use this definition of SB limit throughout the paper. Even though less rigorous than the definition of the SB limits in Li et al. (2011), Ho et al. (2011), and Bakos & Trujillo (2012), this definition captures the depth of an image well in terms of how effectively we can identify faint, merging features.

best sample. The results from the best sample will be provided for the main results (Table 5 and Figures 18 and 19) to demonstrate that the results from both samples are identical.

We also constructed a subsample of AGNs (33) based on the nuclear magnitude cut, which we call as the “best sample.” We have good estimates of nuclear magnitudes from either HST or Canada France Hawaii Telescope (CFHT) images for a subsample of the base sample (59% or 23 out of 39). For the remaining 41% of AGNs, we estimated their nuclear magnitudes using a scaling relation between the black hole mass and the host galaxy bulge luminosity, as described in Section 2.3. For AGNs with good estimates of nuclear magnitudes (59% of the base sample), we find that most of them are dominated by a nuclear component with  $m_{\text{host}} - m_{\text{Nuc}} \sim 1$  mag or  $m_{\text{Nuc}} \sim m_{\text{total}} + 0.36$  mag in median (see Section 3.2). The absolute magnitude cut of  $M_{\text{R}} < -22.6$  corresponds roughly to  $M_{\text{Nuc}}(R) < -22.24$ , assuming the above relation of  $m_{\text{Nuc}} \sim m_{\text{total}} + 0.36$  mag, and we adopt a slightly tighter nuclear magnitude cut of  $M_{\text{Nuc}}(R) < -22.44$  to allow for a margin in the uncertainty in the nuclear magnitude estimates. The best sample will be used to support the validity of the results from the base sample.

Note that AGN host galaxies are mostly early-type galaxies if their nuclear absolute magnitudes in the  $R$  band ( $M_{\text{Nuc}}(R)$ ) are  $M_{\text{Nuc}}(R) \leq -22.44$  mag. Figure 1 shows the histogram of nuclear magnitudes of AGNs divided into two types—galaxies with  $B/T > 0.4$  which we consider as early-type galaxies (Im et al. 2002; Kim & Im 2013), and galaxies with  $B/T < 0.4$ , which can be considered as late-type galaxies. Here, the data are taken from M. Kim et al. (2015, in preparation, hereafter, K15) where they decomposed the surface-brightness profile of AGNs with the HST archival images into host galaxies and the central point source components. Figure 1 indicates that the host galaxies are dominated by early-type galaxies at  $M_{\text{Nuc}}(R) < -22.44$  mag at the  $\sim 86.2\%$  level. However, we did not impose the  $B/T > 0.4$  cut in our AGN selection because the bulge absolute magnitude can be quite uncertain under the presence of a bright nuclear emission, with a typical error of  $\pm 0.2 - 0.4$  mag (Sanchez et al. 2004; Simmons et al. 2008; Kim et al. 2008b). The fraction of AGN hosts with  $B/T < 0.4$  in our sample is small, anyway.

The selection of AGNs was done in roughly two ways, depending on the facilities used, because the observations were performed at one of three observatories (Maidanak, McDonald, and Las Campanas) or the data were taken from the archive (for two AGNs in our study).

For observations at the Maidanak and McDonald observatories or for selecting objects from the archive, AGNs were selected from the Quasars and Active Galactic Nuclei catalog of Véron-Cetty & Véron (2010). Note that the catalog of Véron-Cetty & Véron (2010) provides the absolute B-band magnitude only. In order to convert the B-band absolute magnitude to the R-band magnitude, we assumed a quasar composite spectrum from Vanden Berk et al.

(2001) which gives  $B - R \sim 0.63\text{mag}$ . This value is between 0.46 mag, calculated from the slope  $\alpha_\nu \sim -1.03$  in  $6005 \sim 7180\text{\AA}$  derived by Glikman et al. (2006), and 0.71 mag, calculated from the slope  $\alpha_\nu \sim -1.58$  in  $4000 \sim 8555\text{\AA}$  derived by Vanden Berk et al. (2001). We find 1,103 type-1 AGNs that satisfy the above sample-selection criteria. The absolute magnitudes listed in the Veron-Cetty & Veron catalog, however, may include some amount of the light coming from the host galaxies. Therefore, we opted to observe the PG quasars among the possible targets that are observable during the assigned observing runs at the Maidanak and McDonald observatories because it is known that most of the PG quasars have a strong nuclear component (e.g., Kim et al. 2008a). At the end, the objects were selected mostly from the PG quasar catalog, except for two AGNs for which the data were taken from the CFHT archive. The selected PG quasars were inspected on the Digitized Sky Survey images, and none of them were found to be clearly dominated by a host galaxy component. Then, objects were randomly picked from a prepared target list for the observation. Priority was given during the observations to AGNs with lower redshifts because morphological features become more difficult to identify for higher redshift objects due to the surface brightness dimming and the resolution effects. In total, 18 AGNs of the sample and 14 AGNs of the best sample come from this selection.

The sample observed with the DuPont 2.5-m telescope was taken from the Kim et al. (2008a) and K15 samples, which are made of luminous type-1 AGNs with HST images. Kim et al. (2008a) and K15 assembled an imaging data set from the *HST* archive of type-1 AGNs for which signal-to-noise ratio values of the chosen *HST* images are high enough to disentangle the host galaxy component from the bright nucleus (Kim et al. 2008b). Using the HST images and GALFIT, Kim et al. (2008a) and K15 performed a two-dimensional, multiple-component surface-brightness profile fitting of AGNs, separating the nuclear component from the host galaxy and decomposing the host galaxy surface-brightness profile into a bulge, a disk, and a bar if necessary. The surface-brightness profile fitting provides structural parameters for the host galaxies. Typical uncertainties of  $B/T$  range from 0.05 to 0.2 (see also Ho & Kim 2014). Excluding three AGNs with host galaxies having a clear signature of spiral arms, the number of AGNs that are observed by the DuPont 2.5-m are 21 for the base sample and 19 for the best sample.

Table 1 shows the list of AGNs in the base sample. Figure 2 shows the redshift versus the absolute magnitude of AGNs in the base sample in both  $M_R$  and  $M_{\text{Nuc}}(R)$ . These AGNs span a redshift range of  $0.04 < z < 0.3$ , with a median redshift of  $z = 0.155$ .

In summary, there are 39 and 33 type-1 AGNs at  $z < 0.3$  in the base and the best samples, respectively, where the best sample is based on a more rigorous sample-selection criteria than is the base sample, but at the expense of number statistics. Our base sample

includes all 13 PG quasars with  $M_R < -22.6$  mag,  $z < 0.15$ , and decl.  $> 0$  degree and a total of 23 PG quasars.

## 2.2. Observation and Data Reduction

In order to reveal faint, extended merging features around AGNs, we obtained deep optical images using several facilities. We observed 10 AGNs using SNUCAM (Im et al.2010; FOV=  $18'.1 \times 18'.1$  and pixel scale=  $0''.266$ ) on the 1.5m telescope at the Maidanak observatory in Uzbekistan from 2010 June to 2011 August, six AGNs using the Camera for QUasars in EARly uNiverse (CQUEAN; Park et al. 2012; Kim et al. 2011; Lim et al. 2013; FOV=  $4'.8 \times 4'.8$  and pixel scale=  $0''.281$ ) on the 2.1m telescope at the McDonald observatory in Texas from 2011 February to April, and 21 AGNs using the SITe2K CCD camera of the 2.5m DuPont telescope (FOV=  $8'.85 \times 8'.85$  and pixel scale=  $0''.259$ ) at the Las Campanas observatory from 2008 September to 2009 March. Table 1 gives the summary of the filter, the exposure time, the surface-brightness limit, and the observatory used for the observation of each target. The seeing ranges from  $0''.8$  to  $2''$  with a typical value at around  $1''$ . The adopted filters range from  $V$  through  $i$ , depending on the observatory: The  $V$  band for the SNUCAM data, the  $i$  band for the CQUEAN data, the  $R$  band for the DuPont data, and the  $i$  band or the  $r$  band for CFHT archive data. We avoided using bluer filters (e.g.,  $B$ ) because tidal debris are suggested to be rather red (e.g., Feldmann et al. 2008). Also, the choice of the filter was driven by the observational efficiency to obtain deep images in minimal exposures. For example, CQUEAN at the McDonald observatory is optimized for red wavelengths and the  $r$  band suffers from aberration near the CCD edge, therefore the  $i$  band was chosen. For the Maidanak observation, the balance between faint sky and the desire to avoid a fringing pattern forced us to choose the  $V$  band. Although the chosen filter sets are nonuniform, this is not likely to cause serious systematic errors in our analysis.

Since it is easier to identify merging features at the fainter surface-brightness limit ( $\mu$ ), we tried to reach the surface-brightness limit of  $\sim 27$  mag arcsec $^{-2}$ , comparable to the depth of the control sample. However, the resulting surface-brightness limit is a bit shallower than that of the control sample if the surface brightness dimming is taken into account for objects at  $z \gtrsim 0.1$ . To reach a limit of  $\sim 27$  mag arcsec $^{-2}$ , we observed each target with a series of short exposure frames with exposure times of 60–180s, avoiding saturation of the central point source in the case of the Maidanak images, and a combination of short (a few hundred seconds) and long (1,000–2,000s) exposures for the DuPont images. These frames are combined to create deep images with total exposure times between 1 and 3 hr, after properly rescaling images with different zero points and exposure times so that all of the



frames, before stacking, share the same zero point. In some cases, clear merging features became visible even at a short exposure. In such cases, the observation was stopped before reaching the desired surface-brightness limit (PG 0157+001 and PG 1613+658 at  $\mu \sim 26.11$  and 26.18, respectively). The image of CTS J17.17 from the CFHT archive also shows a tidal tail at  $\mu \sim 26.0$  mag arcsec<sup>-2</sup>.

Figure 3 shows the redshift versus surface-brightness limit of the base sample. Three different symbols represent the three different filters ( $V$ ,  $R$  or  $r$ , and  $i$ ) used for the observation. Note that the surface-brightness limit presented here is the “observed” surface-brightness limit. The surface brightness dimming causes the rest-frame surface-brightness limit of each object to be brighter by  $\sim (1+z)^4$ . This introduces a bias in detecting merging features for an AGN at a higher redshift: our AGN images are shallower than the control sample images for objects at a higher redshift. To indicate this effect, we also plotted with the dotted line the “effective” surface-brightness limit of the control sample. This is a surface-brightness limit of an image when galaxies in the image are assumed to be at a certain redshift. For this line, we adopted the surface-brightness limit of the SDSS Stripe 82 images as 27 mag arcsec<sup>-2</sup> at their median redshift of 0.04. When these images are assumed to be at a given redshift, the surface-brightness limit at that redshift should be  $27 + 10 \log[(1+z)/1.04]$  mag arcsec<sup>-2</sup>. As expected, we find that most of the AGN images are shallower than the dotted line or comparable to the surface-brightness depth within a few tenths of magnitude. We will make a correction for this bias through simulations of AGNs (Section 3.2).

Basic reduction of the images, such as the bias and the dark subtraction, and the flat-fielding was done using the standard IRAF tasks. Flat-field images were taken during twilight, and these were used for flat fielding the images. The dark correction was necessary only for the CQUEAN data where the dark current level is about 0.23 electrons/s/pixel (Park et al. 2012) and not negligible in the data with a long exposure time. The reduced frames were registered to the position of the first frame and stacked using the imcombine task of IRAF. Cosmic rays were rejected during the stacking process, and the bad pixels and columns were fixed by the fixpix task of IRAF before the registration of the frames. The photometry calibration was done by using standard stars observed for the SNUCAM and the DuPont data or by using the photometry information of stars from SDSS in the vicinity of the targets for the CQUEAN data.

### 2.3. Black Hole Masses and Bulge, Nuclear, and Host Luminosities

Because the merging fraction may depend on host-galaxy properties such as black mass or bulge luminosity, we provide these quantities for our AGN sample in Table 1.

The black hole masses,  $M_{\text{BH}}$  in Table 1 are taken from Kim et al. (2008a) and

Vestergaard & Peterson (2006), where  $M_{\text{BH}}$  values are estimated by the reverberation mapping method for nine AGNs (marked as R in Table 1) and by single-epoch methods for 28 AGNs. Here, the single-epoch method refers to the methods that estimate  $M_{\text{BH}}$  values using spectra taken at a single epoch. In such methods, the  $M_{\text{BH}}$  values are derived from a combination of the 5100 Å continuum luminosity and the line widths of broad emission lines (e.g., H $\beta$  or H $\alpha$ ; Vestergaard & Peterson 2006). The  $M_{\text{BH}}$  for the remaining two AGNs are derived from the bulge magnitude of the host, which will be explained in a later part of this section. We caution readers that the absolute values of  $M_{\text{BH}}$  can be off by a certain amount. The  $M_{\text{BH}}$  estimates based on the virial method can be uncertain because they depend on the scaling factor ( $f$ ), which is sensitive to the geometry of the broad line region. Recently, Kormendy & Ho (2013) showed that the correlation between the BH mass and the host galaxy mass in inactive galaxies is tight only for classical bulges and ellipticals. By comparing reverberation-mapped AGN to normal galaxies in the  $M_{\text{BH}} - \sigma_*$  plane only for classical bulges and ellipticals, Ho & Kim (2014) recalibrated the scaling factor, which is approximately two times larger than the value used in this paper. Given the fact that our sample is hosted by early-type galaxies, it is very likely that bulges are either classical or ellipticals. Thus, it is possible that the BH mass is underestimated by a factor of two.

The absolute magnitude of the bulge,  $M_{\text{Bul}}$ , and the central point source,  $M_{\text{Nuc}}$ , are estimated in two ways. In the first method,  $M_{\text{Bul}}$  values are directly estimated from a two-dimensional surface-brightness fitting that takes into account the nuclear, bulge, and disk components. For AGNs with HST images, this is done in Kim et al. (2008a) and K15, and we take the results from their work. Note that the absolute magnitudes of the nuclear component and the bulge component are derived with K corrections that assume a power-law spectral energy distribution for the nuclear component ( $F_\nu \sim \nu^\alpha$  with  $\alpha = -0.44$  blueward of 5,000 Å, and  $-2.45$  otherwise; Vanden Berk et al. 2001) and an empirical template of elliptical galaxies for the bulge component. These absolute magnitudes include the correction for the Galactic extinction (Schlegel et al. 1998). For the AGNs with the ground-based images only, we attempted this procedure for two AGNs with the archival CFHT images because host galaxies are well resolved in these images. We fitted the surface-brightness profile of AGNs using GALFIT (Peng et al. 2002, 2010), assuming a model with three components, a point-spread function (PSF) for the central source and bulge and disk components for the host galaxy. The PSF was derived from a bright star in the vicinity of the AGN ( $< 6'$ ). The disk component is represented by an exponential profile, and the bulge component is fitted with a Sérsic profile (Sersic 1968) as given below:

$$I(r) = I_e \exp[-b_n (r/r_e)^{1/n} - 1], \quad (1)$$

where  $r_e$  is the effective radius,  $I_e$  is the intensity at  $r_e$ , and  $n$  is the Sersic index. During the fitting, the centers of each component were varied, and the background was fixed. We also fitted the object in the vicinity of the target to improve the fitting result. When the scale length of one component is found to be too small ( $< 1$  pixel), we reduced the number of the models (PSF+bulge or PSF+disk) and used the deVaucouleurs profile for the bulge component.

Figure 4 shows the CFHT images of CTS J17.17 and PKS 0159-062 fitted by GALFIT. The tidal tail and the jet-like features can be seen on not only the residual images but also in the original images of the two AGNs. Table 2 shows the resultant fitting parameters. The absolute magnitudes are derived in the same manner as Kim et al. (2008a), which uses an empirical template of an E/S0 galaxy from Calzetti et al. (1994) when deriving the K corrections.

In the second method,  $M_{\text{Bul}}$  is estimated from  $M_{\text{BH}}$  using the correlation between  $M_{\text{Bul}}$  and  $M_{\text{BH}}$  of active galaxies (Kim et al. 2008a) as

$$\log(M_{\text{BH}}/M_{\odot}) = \alpha + \beta M_{\text{Bul}}(R), \quad (2)$$

where  $\alpha = -2.74$  and  $\beta = -0.5$ . Then  $M_{\text{Nuc}}$  is obtained by subtracting this  $M_{\text{Bul}}$  from the total luminosity of the AGN. This procedure assumes that  $M_{\text{Bul}} \sim M_{\text{Host}}$  and thus may overestimate the nuclear luminosity if there is a significant disk component in the host and underestimate the nuclear luminosity if the object is an outlier of Eq. (2). We used this method for six AGNs for which neither HST nor CFHT images were available. These are AGNs with  $M_{\text{BH}}$  values from Vestergaard & Peterson (2006). We used the relation of Kim et al. (2008) instead of the  $M_{\text{BH}}-M_{\text{Bul}}$  correlation of inactive galaxies because host galaxies of AGNs often show signs of a young stellar population (e.g., Kauffmann et al. 2003; Ho & Kim 2014), leading to a somewhat smaller stellar mass-to-light ratio in comparison to inactive galaxies.

Figure 5 shows the redshift versus the BH mass, the Eddington ratio, the bolometric luminosity, and the host bulge magnitude of our sample. Our sample spans parameter spaces of  $10^{7.3}M_{\odot} \sim 10^9M_{\odot}$ ,  $-2 < \log(L_{\text{bol}}/L_{\text{Edd}}) < 0$ ,  $43 < \log(L_{\text{bol}}/L_{\odot}) < 45.5$ , and  $-24 \text{ mag} < M_{\text{Bul}}(R) < -20.5 \text{ mag}$ .

### 3. CONTROL SAMPLE AND SIMULATION OF AGNs

#### 3.1. Control Sample

We look into the merging fraction of AGNs through the presence of a merging feature in AGN host galaxies. To compare it with the merging fraction of inactive galaxies, we construct a control sample. The control sample is restricted to only early-type galaxies because the majority of host galaxies in our luminous AGN sample are early-type galaxies. For the control sample, we chose the SDSS Stripe 82 early-type galaxies with a surface-brightness limit of  $\mu_r = 27 \text{ mag arcsec}^{-2}$  (Kaviraj 2010), which is comparable to or deeper than the image depths of our AGN images (Kaviraj 2010) when taking into account the surface-brightness dimming effect in the images of the AGN sample. There are 317 early-type galaxies in this sample, which is limited to be at  $z < 0.05$  and  $M_r < -20.5 \text{ mag}$ . Table 3 shows the basic properties of the control sample, such as the morphological type,  $B/T$ , and  $M_{\text{BH}}$ .

These early-type galaxies have been classified through careful visual inspection by Kaviraj (2010). The classifications include “relaxed,” “tidal feature,” “dust feature,” “tidal and dust feature,” “interacting,” and “spheroidal galaxy with faint disk features.” Among these classifications, we adopt “tidal feature,” “tidal & dust feature,” and “interacting types” as signs for a merging feature. There are 57 early-type galaxies identified as objects with merging features. A dust feature may be a sign of past merging, but we do not include it as a “merging feature” in our analysis because dust lanes do not extend to the outer region of galaxies and will be extremely difficult to detect in AGNs because a bright point source outshines the dust feature. Note that we simulate AGNs at different redshifts using the control sample in Section 3.2, in order to account for biases arising from a redshift difference between the control and the AGN samples, such as the surface brightness dimming and the change in the sizes of objects. A potential dependence of the merging fraction as a function of luminosity will be removed by analyzing the AGN sample at different host galaxy  $M_{\text{BH}}$  and luminosity bins and taking into account the difference in the  $M_{\text{BH}}$  distribution (Sections 3.2 and 4 and Figure 9).

The median redshift of the Stripe 82 early-type galaxies ( $z_{\text{med}} = 0.04$ ) is lower than that of the AGN sample ( $z_{\text{med}} = 0.15$ ). An evolution in the merging fraction could affect the analysis of the merging fraction difference between the control and the AGN samples, but such an effect is negligible ( $< 20\%$ ), as described below. Earlier works on the study of the merger fraction were controversial, with some studies showing a strong evolution in redshift that goes with  $\sim (1+z)^4$  (e.g., Zepf & Koo 1989; Carlberg et al. 1994; Yee & Ellingson 1995), and with others indicating a weak evolution ( $\sim (1+z)^{1.2}$ ; e.g., Neuschaefer et al.

1997). However, more recent results are converging to a rather weak redshift evolution in the merging fraction of  $(1+z)^{0-2}$  at  $z < 1$  (Lin et al. 2004; Lotz et al. 2008a; Bertone et al. 2009; Bundy et al. 2009; Jogee et al. 2009; Lopez-Sanjuan et al. 2009; Man et al. 2012; Xu et al. 2012), which is especially true for massive or luminous galaxies that are comparable in the mass/luminosity range of the host galaxies studied here (Hsieh et al. 2008; Robaina et al. 2010; ). Even if we adopt the most extreme merging fraction evolution of  $(1+z)^2$  from the recent results, the expected increase in the merging fraction from  $z = 0.04$  to  $z = 0.15$  is only at the level of 20%, which is much smaller than the discrepancy in the merging fraction that we are exploring in this work.

The merging features are further categorized by us into tidal tail (T), shell (S), or interaction (I), as shown in Figure 6. Our definition of “tidal tail” includes tidal tails and disturbed features like loops. The “shell” types are distinguished from “T” types as objects with distorted surface brightness and shell structures, but lacking features like loops. The “interaction” types are objects with their surface-brightness profile extending to a close companion. If there is no merging feature (i.e., “relaxed type” in Kaviraj 2010), we categorize such a case as no feature (N). Although there are quantitative and automatic classification techniques, we adopted the classification through visual inspection because the automatic classification may miss some faint features (Lotz et al. 2008b; Kartaltepe et al. 2010; Adams et al. 2012).

During the visual reinspection of the SDSS Stripe 82 images, we found six galaxies classified as objects with a merging feature in Kaviraj (2010), but we felt that it is not clear whether they really have merging features or not (Figure 7). We treat them in our analysis as early-type galaxies with a merging feature, although we are unlikely to classify AGNs with this kind of object as AGNs with a merging feature.

The bulge magnitudes of the control sample early-type galaxies are taken from the catalog of Simard et al. (2011), who performed a bulge+disk decomposition of galaxies in the SDSS DR7. We adopted the fitted parameters from a model with free Sersic index  $n$  for the bulge component and  $n = 1$  for the disk component. This catalog covers about 84% of the control sample. Simard et al. (2011) did not perform the bulge+disk fitting for the remaining 16% of galaxies because they are brighter than  $m_{\text{petro}}(r) < 14$  mag (too large to fit with within their automated pipeline). For these bright early-type galaxies, we assume that they are bulge-dominated galaxies. Note that the SDSS  $r$ -band magnitude is converted into the R-band magnitude ( $r - R = 0.151$  mag), assuming an elliptical galaxy spectrum of Calzetti et al. (1994). The black hole masses were estimated using Eq. (2), but with the  $\alpha = -2.6$  and  $\beta = -0.5$  of inactive galaxies (Bettoni et al. 2003).

Figure 8 shows the distribution of the bulge absolute magnitudes in  $R$  and the black

hole masses of the control sample as a function of  $z$ . Overplotted in the figures is our AGN sample. Figure 9 compares the  $M_{\text{BH}}$  distribution of the control sample and that of the AGN sample. There is a difference in the overall parameter space covered by the AGN and the control samples, where the  $M_{\text{BH}}$  values of the AGN base sample tend to be brighter and more massive than for the control sample. This difference can introduce a bias in the comparison of merging fractions if the merging fraction changes as a function of host galaxy brightness or black hole mass. Figure 10 shows the merging fraction as a function of  $M_{\text{BH}}$  and  $M_{\text{Bul}}$  of early-type galaxies in the control sample. The error bars indicate 68.3% confidence levels, which are computed using the method described in Cameron (2011)<sup>2</sup>. We find that the merging fraction increases with  $M_{\text{BH}}$  or the bulge luminosity. Therefore, we will take into account the difference in the parameter space ( $M_{\text{BH}}$  or  $M_{\text{Bul}}$ ) between the AGN and the control samples in our analysis, and we will use  $M_{\text{BH}}$  as the reference parameter to adjust for the difference in the covered parameter space. We adopt  $M_{\text{BH}}$  instead of  $M_{\text{Bul}}(R)$ , because it is a better defined quantity for the AGN sample, and the  $M_{\text{BH}}$  versus  $M_{\text{Bul}}$  relation is established more securely for passive galaxies (the control sample) than for AGNs.

### 3.2. Simulation of AGNs Using a Control Sample

It is well known that most (80%) of early-type galaxies show merging features in very deep images ( $\mu \approx 28$  mag arcsec<sup>-2</sup>; van Dokkum 2005), so a careful analysis is needed to analyze AGNs that are associated with merging. The fraction of early-type galaxies with a merging feature is 17% for the control sample (Kaviraj 2010), but there are many factors that can influence the detection rate of a merging feature in the AGN sample.

First, the depth of the image is important because many early-type galaxies with merging features do not reveal merging features in a shallower image. We tried to match the depth of our AGN images and the control sample image, but not perfectly. Most notably, the rest-frame (effective) surface-bright limit of the AGN sample is a bit shallower by 0.5 - 1 mag arcsec<sup>-2</sup> at  $z = 0.2-0.3$  than that of the control sample ( $z_{\text{med}} \sim 0.04$ ) due to the surface brightness dimming.

Second, the AGNs are located farther away than the control sample, so their apparent sizes are smaller. This causes a loss in the resolution element, which can wash away some of the merging features. This resolution effect also needs to be treated properly.

Third, AGNs have bright nuclear components. For AGNs at a very low redshift, the

---

<sup>2</sup>We will use this method to compute errors of fractional quantities throughout the paper.

PSF widths are small compared to the extent of the host galaxy, so the the bright nuclear component does not hamper the detection of a merging feature. However, if they are located at a higher redshift, the width of the PSF becomes comparable to or larger than the host galaxy size, and when combined with an extended wing of the PSF in many ground-based images, low surface-brightness features in the host galaxy becomes difficult to detect.

In order to properly handle these biases, we perform a simulation where we take the control sample early-type galaxy images, plant a nuclear component, and place them at various redshifts. The simulation is done in the following way.

In the first step, early-type galaxy images are block averaged by a factor of 2–5, which corresponds to the change in the angular diameter distance  $D_A(z)$  from  $z = 0.041$  (the median redshift of the control sample) to the redshifts of 0.086, 0.138, 0.2, and 0.275, respectively, matching the redshifts of the AGN sample. The pixel scales of the block-averaged images are all considered as  $0''.3961/\text{pixel}$ , as in the original Stripe 82 image, to properly reflect the redshift changes.

Because the simulated images are block averaged, FWHM of the PSF given in pixel units has shrunk. To mimic the PSF resolution (in arcseconds) of the AGN images, we convolved the block-averaged images using a Gaussian function with a  $\sigma_G$  value as

$$\sigma_G^2 = \sigma_{\text{out}}^2 - \left(\frac{\sigma_{\text{S82}}}{f}\right)^2,$$

where  $\sigma_{\text{S82}}$  is FWHM/2.35 of the image before block averaging,  $f$  is the block-averaging factor, and  $\sigma_{\text{out}}$  is the desired resolution of the output image after the convolution. We adopt two values of  $\sigma_{\text{out}}$  so that the seeing of the resultant image becomes either  $1''$  or  $2''$  in FWHM to allow us to investigate the effect of seeing in the identification of a merging feature.

The pixel values are adjusted so that the total flux of the simulated galaxy is equal to the flux of the galaxy at the desired redshift. During the block-averaging process, the background noise is smoothed out. To make the surface-brightness limit of the resultant image to be  $\sim 27 \text{ mag arcsec}^{-2}$ , additional noises are implemented in the simulated images.

Finally, we plant a point source at the center of the simulated early-type galaxy images in order to mimic an AGN and investigate the effect that a bright AGN component has on the merging fraction analysis. We find that the median of the differences between the host magnitude,  $m_{\text{host}}$ , and the nuclear magnitude,  $m_{\text{Nuc}}$ , is  $(m_{\text{host}} - m_{\text{Nuc}})_{\text{med}} = \sim 1.0 \text{ mag}$ , and the upper and the lower quartiles of the  $m_{\text{host}} - m_{\text{Nuc}}$  values from the mode of the  $m_{\text{host}} - m_{\text{Nuc}}$  distribution are  $\sim 1.5, 0 \text{ mag}$ . To simulate the nuclear point source, we chose a bright star in the SDSS Stripe 82 image and rescaled its pixel values so that the PSF

has three representative values of  $m_{\text{gal}} - m_{\text{Nuc}}$  that are 0, 1.0, and 1.5 mags brighter than the host magnitude. These PSFs are put at the center of the simulated early-type galaxy images.

In summary, we made simulated AGN images for each of 57 SDSS Stripe 82 early-type galaxies with merging features, in a parameter that covers  $z = (0.041, 0.086, 0.138, 0.2, 0.275)$ ,  $m_{\text{Nuc}} = (\text{none}, m_{\text{gal}}, m_{\text{gal}} - 1, m_{\text{gal}} - 1.5)$ , and seeing =  $(1'', 2'')$ , leading to the creation of 40 sets of simulated AGN images per a SDSS Stripe 82 early-type galaxy. Figures 11, 12, 13, 14 show simulated AGN images based on three SDSS Stripe 82 early-type galaxies. Figures 11, 13 are for the seeing of  $1''$ , and Figures 12, 14 are for the seeing of  $2''$ . Redshifts are 0.041, 0.086, 0.138, 0.2, and 0.275 from top to bottom, and the magnitudes of the nuclear point sources are none,  $m_{\text{gal}}$ ,  $m_{\text{gal}} - 1.0$ , and  $m_{\text{gal}} - 1.5$  mags from left to right.

Figure 15 shows quantitatively how the merging features like tidal tails and shells become difficult to identify when the redshifts are changed and the nuclear sources are added. The top panel is for the case that does not include the nuclear point source, and it shows how the redshift effect alone affects the identification of a merging feature. The bottom panel in the figure assumes the addition of a nuclear source with  $m_{\text{gal}} - 1$  mag and a seeing of  $1''$  and shows how the nuclear source makes it more difficult to see the merging features. We find that there is a steady decrease in the identification of a merging feature as we move objects to higher redshifts. With respect to  $z = 0.041$ , only 50% of the features can be identified at  $z = 0.14$ , and this value goes down to 5 – 10% at  $z = 0.2$ . The shell features are more difficult to identify than the tidal features, and all of the shell features are virtually unidentifiable at  $z > 0.2$ . If we include a bright point source, the identification rate of merging features drops by 10 - 20% (or by a factor of two at an intermediate redshift). Our simulation demonstrates that the merging features can disappear easily at a higher redshift and with an addition of a bright nuclear component. Hence, one must take these effects into consideration when comparing the merging fraction of AGNs and with of the control sample galaxies.

## 4. RESULTS

### 4.1. Merging Features in the AGN Sample

Figure 16 shows the images of our AGN sample in the order as listed in Table 1. Using Figure 16, we identified the merging features through visual inspection. The merging features are categorized into tidal tail (T), shell (S), or interaction (I), and no feature (N), as was done for the control sample. The classification of the merging features is indicated in Table 1 and also in Figure 16



Our visual inspection reveals that 17 of 39 AGNs (43.6%) show a merging feature. Among these AGNs with a merging feature, only one AGN shows a shell structure, and another shows a sign of interaction. Therefore, the majority of AGNs showing merging features are categorized as T.

#### 4.2. Merging Fraction: Comparison with Simulated AGNs

In the previous section, we find that 17 of 39 AGNs ( $\sim 43.6\%$ ) show merging features, but only  $\sim 17\%$  of the control sample shows evidence of galaxy mergers. At face value, the merging fraction of AGNs is  $\sim 2.6$  times higher than the merging fraction of the control sample. However, the difference in the merging fraction should be more pronounced if we consider other effects that could make it difficult to identify merging features in the AGN sample. For example, Figures 11 - 14 indicate that it becomes very difficult to identify merging features when an object is at a higher redshift and has a brighter nuclear component. We will take these effects into account and derive a more realistic comparison of the merging fraction between the control and the AGN samples. On the other hand, there are several AGN images that are deeper than the control sample images (the points above the dotted line in Figure 3). For these cases, the noises are added to the AGN images to match the control sample image depth, and the merging feature is classified on the noise-added images. We find that the merging features can be identified in the noise added images, which is not surprising considering that the depths of these AGN images are only a few tenths of magnitude deeper.

Because the merging fraction changes as a function of  $M_{\text{BH}}$  (or equivalently,  $M_{\text{Bul}}(R)$ ), as was shown for the control sample in Figure 10, it is important that we use the control galaxies that have the same properties as the galaxies that AGN hosts evolve into. One could use  $M_{\text{Bul}}(R)$  to tag control galaxies equivalent to an AGN host, but this is not desirable because the growth of AGN hosts has been found to be significant and the exact amount of the evolution is uncertain (e.g., Woo et al. 2006, 2008; Hiner et al. 2012). Moreover, the measurement of  $M_{\text{Bul}}(R)$  is challenging for AGNs with a luminous nuclear component (Sanchez et al. 2004; Simmons et al. 2008; Kim et al. 2008b). Using the  $M_{\text{BH}}$  of an AGN host to identify its counterpart in the control sample is advantageous in this regard because BHs seem to have already grown at  $z \sim 0.3$  in active galaxies, and  $M_{\text{BH}}$  estimators are well established for both AGNs and quiescent galaxies. However, the use of  $M_{\text{BH}}$  is not completely free from difficulties: the intrinsic scatter can be as large as 0.4 dex for  $M_{\text{BH}}$  estimators (e.g., (Peterson et al. 2004)), and BHs could still grow in high  $L_{\text{bol}}/L_{\text{Edd}}$  AGNs (Kim et al. 2008). For the following analysis, we consider  $M_{\text{BH}}$  as a more desirable quantity

to match AGNs with equivalent galaxies in the control sample, but we also present results that use  $M_{\text{Bul}}(R)$  as a galaxy identifier in order to check if the choice of the galaxy identifier can change the main conclusion.

Figure 17 shows the merging fraction of the simulated AGNs as a function of redshift. We divide the sample into two, one with  $\log(M_{\text{BH}}/M_{\odot}) \geq 8.39$  and another with  $\log(M_{\text{BH}}/M_{\odot}) < 8.39$ , because the merging fraction changes as a function of  $M_{\text{BH}}$  as we have shown earlier (Section 3.1). The panels for each  $M_{\text{BH}}$  are also divided into three, each corresponding to a different nuclear magnitude. The magnitudes of the PSF components for each panel are  $m_{\text{gal}}$  (top),  $m_{\text{gal}} - 1.0$  (middle), and  $m_{\text{gal}} - 1.5$  (bottom). The black asterisks are the merging fraction of early-type galaxies without any nuclear component included, and the black open circles are for the cases with a nuclear component included. The seeing of the simulated images is assumed to be  $1''$  here. Tables 4, 5 summarize the merging fractions in the figure, as well as similar numbers for the case of seeing at  $\sim 2''$ .

Figure 17 shows that the merging fraction of the simulated AGNs decreases as a function of redshift, even without adding a nuclear component. At  $z = 0.041$ , it is 17%, but it decreases to 10% at  $z = 0.138$  (a drop of 40%) and to 2% at  $z = 0.275$ . The effect of the addition of the nuclear component becomes prominent when the nuclear component is  $m_{\text{Nuc}} = m_{\text{gal}} - 1$  mag or brighter and at  $z > 0.138$ . At  $z \geq 0.2$ , the merging fraction drops by 50% or more due to the addition of the nuclear component. A larger seeing makes it more difficult to identify merging features. At  $z < 0.2$ , the effect of the seeing is not much, with a decrease in the merging fraction by 20–30%. But at  $z \geq 0.2$ , it could decrease the merging fraction by 50% or more.

In Figure 17, we plot the merging fraction of our AGN sample too (the red stars). The AGN sample is divided into two redshift bins at  $z = 0.155$  to provide enough number statistics in each bin. The horizontal bars on each point show the redshift range covered by the AGNs in each bin. The locations of the red points show the median redshift in each bin. We find that about 40 - 50% of AGNs with  $M_{\text{BH}} \geq 10^{8.39} M_{\odot}$  have merging features regardless of redshift. On the other hand, the merging fraction of AGNs with  $M_{\text{BH}} < 10^{8.39} M_{\odot}$  varies from 60% to 20% going from low to high redshift. Note that the actual merging fraction of AGNs could be higher because the redshift shift and the bright nuclear component can make the merging feature difficult to identify, as we saw from the simulation in the previous section. In comparison to the simulated AGNs, the merging fraction of AGNs is much higher by a factor of 3–10, except for the redshift bin at  $z = 0.12$  of AGNs with massive black holes.

The result is combined into Figure 18, where we plot the merging fraction of AGNs at two different black hole mass bins, and compare it to the same quantity derived for the simulated AGNs (the seeing value of  $1''$  is assumed). The red stars show the merging

fraction of AGNs in the base sample in two mass bins ( $7.3 < \log(M_{\text{BH}}/M_{\odot}) < 8.39$  and  $8.39 \leq \log(M_{\text{BH}}/M_{\odot}) < 9.0$ ). The red filled stars show the merging fraction of AGNs in the best sample. The black filled circles are the merging fraction of the simulated AGNs with  $m_{\text{Nuc}} = m_{\text{gal}} - 1$  mag, i.e., the median of the nuclear magnitudes of the AGN sample, and the black points are plotted at the median  $M_{\text{BH}}$  of each  $M_{\text{BH}}$  bin. When calculating the merging fraction of the simulated AGNs, we use Eq.(3) in order to take into account the difference in the  $M_{\text{BH}}$  distribution between the control sample and the AGN sample (Figure 9), the spread in the redshift distribution of AGNs (Figure 5):

$$\text{Merging fraction} = \frac{\sum_i \sum_j f_{\text{corr}, \delta M_{\text{BH}}(i)} f_{\text{corr}, \delta z(j)} N_{\text{control, merg}}(\delta M_{\text{BH}, i}, \delta z_j)}{\sum_k f_{\text{corr}, \delta M_{\text{BH}}(i)} N_{\text{control}}(\delta M_{\text{BH}, i})} \quad (3)$$

Here, the quantity  $N_{\text{control, merg}}(\delta M_{\text{BH}, i}, \delta z_j)$  is the number of simulated AGNs that are identified to have merging features with their  $M_{\text{BH}}$  and redshifts belonging to an  $M_{\text{BH}}$  bin of  $\delta M_{\text{BH}, i}$  (e.g.,  $8.25 < \log(M_{\text{BH}}/M_{\odot}) < 8.5$ ) and a redshift bin of  $\delta z_j$ , and  $N_{\text{control}}(\delta M_{\text{BH}, i})$  is the total number of control galaxies in the mass bin of  $\delta M_{\text{BH}, i}$ . The factors  $f_{\text{corr}, \delta M_{\text{BH}}(i)}$  and  $f_{\text{corr}, \delta z(j)}$  correct for the difference in the  $M_{\text{BH}}$  distribution between the AGN and the control samples and account for a range of redshifts of AGNs. They are defined as  $f_{\text{corr}, \delta M_{\text{BH}}(i)} = [N_{\text{control}}(\Delta M_{\text{BH}})/N_{\text{control}}(\delta M_{\text{BH}, i})] \times [N_{\text{AGN}}(\delta M_{\text{BH}, i})/N_{\text{AGN}}(\Delta M_{\text{BH}})]$  and

$f_{\text{corr}, \delta z(j)} = N_{\text{AGN}}(\delta z_j, \Delta M_{\text{BH}})/N_{\text{AGN}}(\Delta M_{\text{BH}})$ , where  $\Delta M_{\text{BH}}$  represents either one of the two broad mass bins of  $7.3 < \log(M_{\text{BH}}/M_{\odot}) < 8.39$  and  $8.39 \leq \log(M_{\text{BH}}/M_{\odot}) < 9.0$ .

Irrespective of whether we adopt the base or the best sample, we find the following (Table 6). At the higher mass bin of  $8.39 \leq \log(M_{\text{BH}}/M_{\odot}) < 9.0$ , the AGN merging fraction is about  $48 \pm 15\%$ , and it is  $12 \pm 5\%$  for the simulated AGNs, which is a difference of a factor of four. At the lower mass bin of  $7.3 < \log(M_{\text{BH}}/M_{\odot}) < 8.39$ , the AGN fraction is about 39%, and that of the simulated AGNs is only  $5 \pm 2\%$ , giving a factor of eight difference.

Similarly, we plot the merging fraction as a function of the absolute magnitude of the bulge (Figure 19). The same method is adopted for computing the merging fraction as for the  $M_{\text{BH}}$ -based merging fractions but using  $M_{\text{Bul}}(R)$  as a quantity to compute the correction factor. We find exactly the same trend as in Figure 18, although the difference in the merging fraction between the control and the AGN samples is reduced in at the lower luminosity bin (with respect to the lower  $M_{\text{BH}}$  bin). The reason for the discrepancy can be understood when we examine the difference in the overall distribution of AGNs in  $M_{\text{BH}}$  versus  $M_R$  with respect to the control sample, as seen in Figure 8. In  $M_R$ , most AGNs occupy the luminous end of the control sample, while it is less so in  $M_{\text{BH}}$ . Luminous early types in the control

sample have a higher merging fraction than fainter early types, which leads to the higher merging fraction at the lower luminosity bin of the control sample. However, the amount of luminosity evolution is uncertain for early-type host galaxies of AGNs, and the amount of luminosity dimming can be well above a few tenths of the magnitude of normal early-type galaxies (e.g., Im et al. 1996, 2002; Bernardi et al. 2003) from  $z = 0.3$  to 0.04. If we make such a correction for the luminosity dimming in the AGN host galaxy, the  $M_R$  distribution would resemble the  $M_{\text{BH}}$  distribution more closely, and the merging fraction of the control galaxies at the lower luminosity bin would decrease to the level of the value for the lower  $M_{\text{BH}}$  bin.

We note that our classification using visual inspection is not likely to affect our result. To quantify possible errors in the visual classification, the visual classification was done by two authors independently for the simulated AGN sample. We find that the classification agrees fairly well, and the resultant error in the merging fraction is only about  $\pm 0.01$  to  $\pm 0.03$ . Overall, this is a negligible amount.

We also note that a slight difference in the redshift ranges of the control sample and the AGN sample does not bias our result in favor of higher merging fraction in the AGN sample. As we already argued in Section 3.1, the merging fraction evolves only mildly over the redshift range of  $z = 0.15$  and  $z = 0.04$ . The redshift evolution trend can be reduced by limiting our AGN sample to those at  $z < 0.1$ . Doing so only makes our result stronger, with five out of six AGNs at  $z < 0.1$  showing merging features.

When defining our sample, we excluded AGN hosts with spiral arms when HST images are available. We could not do so for AGNs whose images come from the ground-based observation. This can lead to a slight underestimate of the AGN merging fraction because AGN hosts with spiral arms (i.e., a significant disk component) tend to have small  $M_{\text{BH}}$  values and therefore a smaller merging fraction than those with large  $M_{\text{BH}}$  values.

Although we find that 43.6% of luminous AGNs in our sample show merging features, our simulation of AGNs using the control sample strongly suggests that this is more likely a lower limit of the merging fraction. The true merging fraction of the luminous AGNs can be estimated by using the simulation result. We have shown earlier that the merging fraction is reduced by a factor of 1.7–7.6 at  $z = 0.15$  to  $z = 0.2$  with respect to the merging fraction at  $z = 0.041$ . If we make this correction to the observed merging fraction of AGNs, then the merging fraction becomes about 75–100%. Overall, we conclude that the merging is closely related to luminous AGN activity and very much likely to be the triggering mechanism of luminous AGNs.

## 5. DISCUSSION

Tidal tails can be more prominent in gas-rich “wet merging” (Feldmann et al. 2008) and appear from an early stage of galaxy merging (Mihos 1995). As the disturbed gaseous and stellar materials fall back to the merger product, the tidal tail shrinks and the fall-back material can form shell-like or loop-like structures (Mihos 1995; Feldmann et al. 2008). Therefore, we subdivided the merging feature into the tidal-tail type (early stage of merging), the shell type (late stage of merging), and the interaction type (very early stage of the merging), as an attempt to see which stage of the merging our AGN hosts are found. We find that only one of 17 AGNs with a merging feature shows the shell structure. On the other hand, the majority of AGNs with merging features (15 out of 17) are in the category of the tidal tail type, and the remaining one is the interaction type. In comparison,  $\sim 25\%$  of galaxy mergers in the control sample show the shell structure. At a first glance, this result appears to be in perfect agreement with the merger-triggered AGN scenario. However, we have shown through our simulation that shell structures are difficult to identify when objects are farther away and have a bright central point source. For example, three of our AGNs are also studied in Bennert et al. (2008), and they show that two of them (MC 1635+119 and PKS 0736+01) have a shell-type feature in their HST images, but we do not see such a feature in our low-resolution ground-based image, clearly indicating that we are missing the shell-type merging features in some cases. Therefore, we conclude that the lack of tidal-feature-type AGNs in our sample is consistent with a merger-triggered AGN scenario, but a firm conclusion on this issue should be obtained through future studies with deeper and higher resolution images of AGNs (e.g., Bennert et al. 2008).

We mentioned earlier that we could not identify merging features for some control galaxies that have been marked as early types with merging features in Kaviraj (2010). Consequently, such objects would not be classified to have a merging feature even if they exist in the AGN sample. A correction to this difference in the merging feature classification between classifiers (Kaviraj vs. us) could only more strongly in favor of our result.

Because some of our AGNs overlap with those studied in previous works, we can make a direct comparison of the classification between ours and the other works. We find that 18 objects in our AGN sample overlap with the AGN hosts studied by Hutchings & Neff (1992), Bahcall et al. (1997), McLure et al. (1999), Dunlop et al. (2003), Bennert et al. (2008), and Letawe et al. (2010). These studies are based on either HST images or ground-based images. We find that three AGNs in the overlap sample are classified to have merging features in our study (PKS 1020-103, PKS 2355-082, and PG 1302-102), but they are mentioned only as objects with companions in the other studies, demonstrating that our deep images newly uncovered faint merging features in some AGNs. On the other hand, we miss two AGNs with

a shell-type merging feature as mentioned above, showing that our images are not sensitive to picking up smooth, symmetric, low surface features with detailed structures such as shells. One object, PG 0052+251, was classified as Sb in Bahcall et al. (1997), but we classify it as a tidal-tail type. The spiral structure is mentioned to be terminated at a companion galaxy in Dunlop et al. (2003), so the spiral structure may be related to a merging activity. The bulge+disk decomposition of the host surface-brightness profile indicates that  $B/T = 0.67$  (K15), suggesting that the host galaxy is an early-type galaxy, lending a farther support that the spiral structure is related to the past merging activity. Our classification agrees with that of previous works for the remaining 12 AGNs in the overlap sample.

Finally, we comment on the contradictory observational results regarding the AGN triggering mechanism. Our results that merging features are much more frequently found in luminous AGNs than in quiescent galaxies, and that the AGN merging fraction could be as high as 75%–100%, point toward a strong connection between merging and luminous AGN activity. Our AGN sample spans a range of  $10^{44} \text{ergs}^{-1} < L_{\text{bol}} < 10^{45.4} \text{ergs}^{-1}$  with a median bolometric luminosity of  $L_{\text{bol}} \sim 10^{44.52} \text{ergs}^{-1}$ , and the AGN samples of studies that have not found merging evidence in AGNs extend to a much fainter luminosity range ( $L_{\text{bol}} \sim 10^{42} \text{ergs}^{-1}$ ). Therefore, the difference in the explored luminosity range could be the main source of the discrepancy, as suggested in previous works such as Treister et al. (2012), Hopkins & Hernquist (2009), and Draper & Ballantyne (2012) that major merging is only dominant in luminous AGNs. This leads us to a question whether fainter AGNs are really triggered by an internal mechanism. After all, SMBHs are predominantly found in bulges of spiral galaxies that are the main hosts of faint AGNs. However, bulges of late-type galaxies can also be produced through merging (Aguerri et al. 2001; Kannappan et al. 2004; Eliche-Moral et al. 2006; Hopkins et al. 2010; Scannapieco et al. 2010; Oser et al. 2012). Then, if the production of the bulges is closely connected to AGN activity, much like in the case of major merging-triggered AGNs, merging features from merging events (possibly minor merging) could be detectable in less luminous AGNs too. The tidal tails from faint satellite galaxies are going to be much less prominent than the tidal tails associated with major mergers in luminous AGNs, simply if the brightness of tidal tails scales with host galaxy luminosity. Thus, images that go deeper than current survey limits may reveal traces of the past minor merging activities in less luminous AGNs.

For example, studies based on HST survey images have shown little evidence for merging activities in less luminous AGNs. Such imaging data, although very deep in detecting point sources, suffer in depth when the surface-brightness limit is considered. This is largely due to the surface brightness dimming effect that scales as  $\sim (1+z)^4$ . In the case of the CANDELS survey (Grogin et al. 2011; Koekemoer et al. 2011) and the images that were used by Schawinski et al. (2012) to draw a conclusion that only 4% of AGNs at  $z \sim 2$

went through major merging, the SB limit is only 25.4 AB mag arcsec<sup>-2</sup> at F775W (similar to  $R$  band) when the SB dimming correction is made. Future studies with deeper imaging data will certainly tell us whether the AGN triggering mechanism is closely related to the formation mechanism of bulges. If the classical bulges are formed through merging but the pseudobulges are formed through an internal mechanism (e.g., Kormendy & Ho 2013), such a difference will be reflected in the existence or nonexistence of merging features around luminous AGNs and in the photometric properties of bulges.

## 6. SUMMARY

To investigate whether galaxy merging can trigger AGN activity or not, we examined deep images (surface-brightness limit of  $\mu$  of  $\sim 27$  mag arcsec<sup>-2</sup>) of 39 luminous AGNs at  $M_R < -22.6$ ,  $z < 0.3$ , and  $7.3 < \log(M_{\text{BH}}/M_{\odot}) < 9.0$ . We find that 17 of 39 AGNs ( $\sim 43.6\%$ ) show evidence of galaxy mergers such as tidal tail, shell, and interaction through careful visual inspection. Compared to the control sample of early-type galaxies taken from the SDSS Stripe 82 data at a similar surface-brightness limit, the fraction of AGNs showing the merging feature is about 2.6 times higher. This difference becomes more significant when we simulate AGNs using the SDSS Stripe 82 early-type galaxy images because our AGNs are located farther away than the SDSS Stripe 82 galaxies (surface brightness dimming), and also bright nuclear components of AGNs can make it more difficult to detect merging features. Overall, we find that the merging fraction of the simulated AGNs is only 5–15%, much smaller than our result by factors of 4–8 depending on  $M_{\text{BH}}$  values. Our result strongly suggests that merging plays an important role in triggering AGN activity of luminous AGNs. Future studies with deep imaging observation of fainter AGNs are needed to understand how AGN activities are triggered in fainter AGNs.

This work was supported by the Creative Initiative program, No. 2008-0060544, of the National Research Foundation of Korea (NRFK) funded by the Korean government (MSIP). We thank our CEOU/SNU colleagues for useful discussion and taking some of the data used in this work, and the staffs of the McDonald Observatory, the Maidanak Observatory, and the Las Campanas Observatory for their assistance during the observations. We appreciate useful comments from an anonymous referee. This paper includes the data taken at the McDonald Observatory of The University of Texas at Austin, the Maidanak Observatory, and the Las Campanas Observatory of the Carnegie Institution for Science. MK acknowledges the support from a KASI-Carnegie fellowship. LCH acknowledges support from the Kavli Foundation, Peking University, the Chinese Academy of Sciences, and the Carnegie Institution for Science.

## REFERENCES

- Adams, S. M., Zaritsky, D., Sand, D. J., et al. 2012, *AJ*, 144, 128
- Aguerri, J. A. L., Balcells, M., & Peletier, R. F. 2001, *A&A*, 367, 428
- Athanassoula, E. 2003, *MNRAS*, 341, 1179
- Bahcall, J. N., Kirhakos, S., Saxe, D. H., & Schneider, D. P. 1997, *ApJ*, 479, 642
- Bakos, J., & Trujillo, I. 2012, arXiv:1204.3082
- Barnes, J. E., & Hernquist, L. E. 1991, *ApJ*, 370, L65
- Barnes, J. E., & Hernquist, L. 1992, *ARA&A*, 30, 705
- Bernardi, M., Sheth, R. K., Annis, J., et al. 2003, *AJ*, 125, 1866
- Bennert, N., Canalizo, G., Jungwiert, B., et al. 2008, *ApJ*, 677, 846
- Bertone, S., & Conselice, C. J. 2009, *MNRAS*, 396, 2345
- Bessiere, P. S., Tadhunter, C. N., Ramos Almeida, C., & Villar Martín, M. 2012, *MNRAS*, 426, 276
- Bettoni, D., Falomo, R., Fasano, G., & Govoni, F. 2003, *A&A*, 399, 869
- Bournaud, F., & Combes, F. 2002, *A&A*, 392, 83
- Bradshaw, E. J., Almaini, O., Hartley, W. G., et al. 2011, *MNRAS*, 415, 2626
- Bullock, J. S., & Johnston, K. V. 2005, *ApJ*, 635, 931
- Bundy, K., Fukugita, M., Ellis, R. S., et al. 2009, *ApJ*, 697, 1369
- Cameron, E. 2011, *PASA*, 28, 128
- Calzetti, D., Kinney, A. L., & Storchi-Bergmann, T. 1994, *ApJ*, 429, 582
- Carlberg, R. G., Pritchet, C. J., & Infante, L. 1994, *ApJ*, 435, 540
- Carpinetti, A., Kaviraj, S., Darg, D., et al. 2012, *MNRAS*, 420, 2139
- Cisternas, M., Jahnke, K., Inskip, K. J., et al. 2011, *ApJ*, 726, 57
- Combes, F., & Gerin, M. 1985, *A&A*, 150, 327



- Darg, D. W., Kaviraj, S., Lintott, C. J., et al. 2010, *MNRAS*, 401, 1552
- Draper, A. R., & Ballantyne, D. R. 2012, *ApJ*, 753, L37
- Dunlop, J. S., McLure, R. J., Kukula, M. J., et al. 2003, *MNRAS*, 340, 1095
- Eliche-Moral, M. C., Balcells, M., Aguerri, J. A. L., & González-García, A. C. 2006, *A&A*, 457, 91
- Ellison, S. L., Patton, D. R., Mendel, J. T., & Scudder, J. M. 2011, *MNRAS*, 418, 2043
- Feldmann, R., Mayer, L., & Carollo, C. M. 2008, *ApJ*, 684, 1062
- Ferrarese, L., & Ford, H. 2005, *Space Sci. Rev.*, 116, 523
- Georgakakis, A., Coil, A. L., Laird, E. S., et al. 2009, *MNRAS*, 397, 623
- Glikman, E., Helfand, D. J., & White, R. L. 2006, *ApJ*, 640, 579
- Grogin, N. A., Kocevski, D. D., Faber, S. M., et al. 2011, *ApJS*, 197, 35
- Heller, C. H., & Shlosman, I. 1994, *ApJ*, 424, 84
- Hernquist, L., & Spergel, D. N. 1992, *ApJ*, 399, L117
- Hiner, K. D., Canalizo, G., Wold, M., Brotherton, M. S., & Cales, S. L. 2012, *ApJ*, 756, 162
- Ho, L. C., & Kim, M. 2014, *ApJ*, 789, 17
- Ho, L. C., Li, Z.-Y., Barth, A. J., Seigar, M. S., & Peng, C. Y. 2011, *ApJS*, 197, 21
- Hopkins, P. F., Hernquist, L., Martini, P., et al. 2005, *ApJ*, 625, L71
- Hopkins, P. F., & Hernquist, L. 2009, *ApJ*, 694, 599
- Hopkins, P. F., Bundy, K., Croton, D., et al. 2010, *ApJ*, 715, 202
- Hsieh, B. C., Yee, H. K. C., Lin, H., Gladders, M. D., & Gilbank, D. G. 2008, *ApJ*, 683, 33
- Hutchings, J. B., & Neff, S. G. 1992, *AJ*, 104, 1
- Im, M., Griffiths, R. E., Ratnatunga, K. U., & Sarajedini, V. L. 1996, *ApJ*, 461, L79
- Im, M., Griffiths, R. E., & Ratnatunga, K. U. 1997, *ApJ*, 475, 457
- Im, M., Simard, L., Faber, S. M., et al. 2002, *ApJ*, 571, 136

- Im, M., Ko, J., Cho, Y., et al. 2010, *Journal of Korean Astronomical Society*, 43, 75
- Jogee, S., Miller, S. H., Penner, K., et al. 2009, *ApJ*, 697, 1971
- Kannappan, S. J., Jansen, R. A., & Barton, E. J. 2004, *AJ*, 127, 1371
- Karouzos, M., Jarvis, M. J., & Bonfield, D. 2014a, *MNRAS*, 439, 861
- Karouzos, M., Im, M., Kim, J.-W., et al. 2014b, *ApJ*, 797, 26
- Kartaltepe, J. S., Sanders, D. B., Le Floch, E., et al. 2010, *ApJ*, 721, 98
- Kauffmann, G., Heckman, T. M., Tremonti, C., et al. 2003, *MNRAS*, 346, 1055
- Kaviraj, S. 2010, *MNRAS*, 406, 382
- Kim, D., & Im, M. 2013, *ApJ*, 766, 109
- Kim, E., Park, W.-K., Jeong, H., et al. 2011, *Journal of Korean Astronomical Society*, 44, 115
- Kim, M., Ho, L. C., Peng, C. Y., et al. 2008, *ApJ*, 687, 767
- Kim, M., Ho, L. C., Peng, C. Y., Barth, A. J., & Im, M. 2008, *ApJS*, 179, 283
- Kim, T., Sheth, K., Hinz, J. L., et al. 2012, *ApJ*, 753, 43
- Kocevski, D. D., Faber, S. M., Mozena, M., et al. 2012, *ApJ*, 744, 148
- Koekemoer, A. M., Faber, S. M., Ferguson, H. C., et al. 2011, *ApJS*, 197, 36 *Astrophysics of Gravitational Wave Sources*, 686, 161
- Komossa, S. 2003, *AIP Conf. Proc. 686, The Astrophysics of Gravitational Wave Sources*, ed. J. Centrella (Melville, NY, AIP), 161
- Kormendy, J., & Richstone, D. 1995, *ARA&A*, 33, 581
- Kormendy, J., & Ho, L. C. 2013, *ARA&A*, 51, 551 Peterson, B. M., Ferrarese, L., Gilbert, K. M., et al. 2004, *ApJ*, 613, 682
- Koss, M., Mushotzky, R., Treister, E., et al. 2011, *ApJ*, 735, L42
- Koulouridis, E., & Plionis, M. 2010, *ApJ*, 714, L181
- Krick, J. E., Bernstein, R. A., & Pimbblet, K. A. 2006, *AJ*, 131, 168

- Lee, G.-H., Woo, J.-H., Lee, M. G., et al. 2012, *ApJ*, 750, 141
- Letawe, Y., Letawe, G., & Magain, P. 2010, *MNRAS*, 403, 2088
- Li, Z.-Y., Ho, L. C., Barth, A. J., & Peng, C. Y. 2011, *ApJS*, 197, 22
- Lim, J., Chang, S., Pak, S., Kim, Y., Park, W.-K., & Im, M. 2013, *Journal of Korean Astronomical Society*, 46, 161
- Lin, L., Koo, D. C., Willmer, C. N. A., et al. 2004, *ApJ*, 617, L9
- López-Sanjuan, C., Balcells, M., Pérez-González, P. G., et al. 2009, *A&A*, 501, 505
- Lotz, J. M., Davis, M., Faber, S. M., et al. 2008, *ApJ*, 672, 177
- Lotz, J. M., Jonsson, P., Cox, T. J., & Primack, J. R. 2008, *MNRAS*, 391, 1137
- Lynden-Bell, D. 1979, *MNRAS*, 187, 101
- Man, A. W. S., Toft, S., Zirm, A. W., Wuyts, S., & van der Wel, A. 2012, *ApJ*, 744, 85
- McLure, R. J., Kukula, M. J., Dunlop, J. S., et al. 1999, *MNRAS*, 308, 377
- Mihos, J. C. 1995, *ApJ*, 438, L75
- Mihos, J. C., & Hernquist, L. 1996, *ApJ*, 464, 641
- Neuschaefer, L. W., Im, M., Ratnatunga, K. U., et al. 1997, *ApJ*, 480, 59
- Oh, S., Oh, K., & Yi, S. K. 2012, *ApJS*, 198, 4
- Oser, L., Naab, T., Ostriker, J. P., & Johansson, P. H. 2012, *ApJ*, 744, 63
- Park, W.-K., Pak, S., Im, M., et al. 2012, *PASP*, 124, 839
- Peng, C. Y., Ho, L. C., Impey, C. D., & Rix, H.-W. 2002, *AJ*, 124, 266
- Peng, C. Y., Ho, L. C., Impey, C. D., & Rix, H.-W. 2010, *AJ*, 139, 2097
- Peterson, B. M., Ferrarese, L., Gilbert, K. M., et al. 2004, *ApJ*, 613, 682
- Pfenniger, D., & Friedli, D. 1991, *A&A*, 252, 75
- Quinn, P. J. 1984, *ApJ*, 279, 596
- Ramos Almeida, C., Bessiere, P. S., Tadhunter, C. N., et al. 2012, *MNRAS*, 419, 687

- Robaina, A. R., Bell, E. F., van der Wel, A., et al. 2010, *ApJ*, 719, 844
- Sakamoto, K., Okumura, S. K., Ishizuki, S., & Scoville, N. Z. 1999, *ApJ*, 525, 691
- Sanchez, S. F., Jahnke, K., Wisotzki, L, et al. 2004, *ApJ*, 614, 586
- Sanders, D. B., Soifer, B. T., Elias, J. H., et al. 1988, *ApJ*, 325, 74
- Sanders, D. B., Soifer, B. T., Elias, J. H., Neugebauer, G., & Matthews, K. 1988, *ApJ*, 328, L35
- Scannapieco, C., Gadotti, D. A., Jonsson, P., & White, S. D. M. 2010, *MNRAS*, 407, L41
- Schawinski, K., Thomas, D., Sarzi, M., et al. 2007, *MNRAS*, 382, 1415
- Schawinski, K., Simmons, B. D., Urry, C. M., Treister, E., & Glikman, E. 2012, *MNRAS*, 425, L61
- Schawinski, K., Treister, E., Urry, C. M., et al. 2011, *ApJ*, 727, L31
- Schlegel, D. J., Finkbeiner, D. P., & Davis, M. 1998, *ApJ*, 500, 525
- Sellwood, J. A. 1981, *A&A*, 99, 362 Argentina: Observatorio Astronomico, 1968,
- Sersic, J. L. 1968, *Atlas de Galaxias Australes*, Cordoba, Argentina: Obs. Astron. Univ. Nacional de Cordova
- Sheen, Y.-K., Yi, S. K., Ree, C. H., & Lee, J. 2012, *ApJS*, 202, 8
- Simmons, B. D., Urry, C. M., Schawinski, K., Cardamone, C., & Glikman, E. 2012, arXiv:1211.0278
- Simmons, B. D., & Urry, C. M. 2008, *ApJ*, 683, 644
- Silverman, J. D., Kampczyk, P., Jahnke, K., et al. 2011, *ApJ*, 743, 2
- Simard, L., Trevor Mendel, J., Patton, D. R., Ellison, S. L., & McConnachie, A. W. 2011, *VizieR Online Data Catalog*, 219, 60011
- Springel, V., Di Matteo, T., & Hernquist, L. 2005, *ApJ*, 620, L79
- Tal, T., van Dokkum, P. G., Nelan, J., & Bezanson, R. 2009, *AJ*, 138, 1417
- Toomre, A., & Toomre, J. 1972, *ApJ*, 178, 623
- Treister, E., Schawinski, K., Urry, C. M., & Simmons, B. D. 2012, *ApJ*, 758, L39

- Urrutia, T., Lacy, M., & Becker, R. H. 2008, *ApJ*, 674, 80
- van Albada, G. D., & Roberts, W. W., Jr. 1981, *ApJ*, 246, 740
- Vanden Berk, D. E., Richards, G. T., Bauer, A., et al. 2001, *AJ*, 122, 549
- van Dokkum, P. G. 2005, *AJ*, 130, 2647
- Véron-Cetty, M.-P., & Véron, P. 2010, *A&A*, 518, A10
- Vestergaard, M., & Peterson, B. M. 2006, *ApJ*, 641, 689
- Villforth, C., Hamann, F., Koekemoer, A., et al. 2013, arXiv:1303.1874
- Xu, C. K., Zhao, Y., Scoville, N., et al. 2012, *ApJ*, 747, 85
- Yee, H. K. C., & Ellingson, E. 1995, *ApJ*, 445, 37
- Woo, J., Treu, T., Malkan, M. A., & Blanford, R. D. 2006, *ApJ*, 645, 900
- Woo, J., Treu, T., Malkan, M. A., & Blanford, R. D. 2008, *ApJ*, 681, 925
- Zepf, S. E., & Koo, D. C. 1989, *ApJ*, 337, 34

Table 1. AGN Sample

Name	$z$	$m_V$	$M_R$	$M_{\text{BH}}^a$	Ref.	$M_{\text{Nuc}}^b$	$M_{\text{Bul}}^c$	$M_{\text{Host}}^d$	$\frac{L_{\text{bol}}}{L_{\text{Edd}}}$	Filter	Exp.	$\mu$	Seeing	Tel.	Merging
(1)	(2)	(mag)	(mag)	( $M_{\odot}$ )	(6)	(mag)	(mag)	(mag)	( $\text{erg s}^{-1}$ )	(11)	(s)	( $\text{mag}/''^2$ )	(arcsec)	(15)	Type
3C 206	0.2	15.76	-24.67	8.6	S(Kim)	-23.94	-22.01	-22.01	0.204	R	3600	26.61	0.9	D	N
CTS J17.17	0.11	15.9	-23.27	8.3	-	-21.57	-22.07	-23.27	-	i	920	26.00	0.93	C	T
FAIRALL 9	0.05	13.83	-22.86	8.2	R(Kim)	-18.97	-21.27	-21.66	0.013	R	1400	26.83	1.47	D	T
HB 890316-346	0.27	15.1	-25.97	8.9	S(Kim)	-24.5	-22.91	-23.21	0.043	R	1080	25.09	0.96	D	T
HE 0306-3301	0.25	15.8	-25.27	7.9	S(Kim)	-24.63	-21.08	-22.57	0.573	R	2640	27.47	1.13	D	N
HE 0354-5500	0.27	15.7	-25.57	7.9	S(Kim)	-24.49	-23.31	-23.51	0.516	R	4800	26.10	1.12	D	N
HE 1434-1600	0.14	15.5	-23.87	8.6	S(Kim)	-23.39	-22.45	-22.45	0.040	R	3600	27.18	0.79	D	T
MC 1635+119	0.15	16.5	-22.77	7.9	S(Kim)	-21.27	-22.49	-22.49	0.05	R	3600	27.57	0.92	D	N
OX 169	0.21	15.73	-24.67	8.5	S(Kim)	-24.5	-22.95	-23.12	0.19	R	3080	26.92	1.25	D	T
PG 0026+12	0.15	15.41	-23.97	8.3	R(Kim)	-24.12	-22.37	-22.37	0.261	V	9180	26.96	1.55	Ma	N
PG 0052+251	0.16	15.43	-24.47	8.3	R(Kim)	-24.12	-22.62	-23.02	0.179	V	9360	26.89	1.21	Ma	T
PG 0157+001	0.16	15.87	-23.87	7.8	S(Kim)	-22.64	-23.65	-23.94	0.529	V	5400	26.11	1.15	Ma	T
PG 0844+349	0.06	14.5	-23.06	7.7	R(Kim)	-23.46	-21.79	-22.11	0.412	i	14400	27.40	2.08	Mc	T
PG 1004+130	0.24	15.68	-25.07	8.9	S(Kim)	-25.59	-23.94	-23.95	0.107	R	3200	27.22	0.74	D	N
PG 1114+445	0.14	16.12	-23.37	8.6	S(V&P)	-22.44	-22.68	-22.68	-	i	10800	27.52	2.08	Mc	N
PG 1116+215	0.18	14.72	-25.37	8.2	S(Kim)	-24.77	-23.29	-23.29	0.482	R	3600	26.65	0.95	D	N
PG 1211+143	0.08	14.19	-23.97	7.9	R(Kim)	-23.84	-21.39	-21.67	0.286	R	3600	27.74	1.11	D	N
PG 1302-102	0.28	14.92	-26.08	8.6	S(Kim)	-26.09	-23.98	-23.99	0.403	R	3600	26.86	0.84	D	T
PG 1307+085	0.16	15.89	-23.87	8.4	R(Kim)	-24.05	-22.25	-22.25	0.106	R	3600	26.90	0.93	D	N
PG 1309+355	0.18	15.64	-24.67	8.4	S(Kim)	-24.63	-23.63	-23.63	0.176	V	10980	27.29	1.63	Ma	N
PG 1322+659	0.17	15.84	-24.07	8.3	S(V&P)	-23.83	-22.06	-22.06	-	V	11100	27.75	1.83	Ma	N
PG 1351+64	0.09	14.28	-23.97	8.5	S(Kim)	-23.44	-22.18	-22.27	0.075	V	9720	27.41	1.91	Ma	N
PG 1352+183	0.15	16.68	-22.97	8.4	S(V&P)	-21.88	-22.34	-22.34	-	V	10800	27.15	1.86	Ma	N
PG 1402+261	0.17	15.34	-24.57	7.5	S(Kim)	-23.23	-21.17	-22.51	0.486	V	12960	27.06	1.47	Ma	N
PG 1411+442	0.09	14.01	-24.57	8.4	R(Kim)	-23.6	-21.54	-22.3	0.076	i	12600	27.40	2.54	Mc	T
PG 1416-129	0.13	16.1	-22.97	8.5	S(Kim)	-22.82	-21.59	-21.59	0.044	R	2400	27.37	0.92	D	N
PG 1440+356	0.08	14.58	-23.37	7.4	S(Kim)	-23.19	-20.91	-22.17	0.608	V	7550	27.52	1.17	Ma	T
PG 1519+226	0.14	16.5	-22.97	7.9	S(V&P)	-22.66	-21.38	-21.38	-	i	9000	27.57	2.08	Mc	N
PG 1613+658	0.13	15.49	-23.37	8.2	R(Kim)	-24.32	-23.08	-24.08	0.297	i	5400	26.18	2.02	Mc	T
PG 1617+175	0.11	15.39	-23.37	8.7	R(Kim)	-23.22	-21.21	-21.38	0.029	R	3600	27.41	0.88	D	N
PG 1626+554	0.13	15.68	-23.67	8.5	S(V&P)	-23.22	-22.5	-22.5	-	i	6000	27.32	2.54	Mc	N
PG 2214+139	0.07	14.66	-22.96	8.6	S(V&P)	-21.56	-22.61	-22.61	-	V	10800	27.36	1.1	Ma	S
PKS 0159-062	0.19	16.6	-23.17	8.7	-	-20.94	-22.87	-22.9	-	r	2180	27.96	0.73	C	T
PKS 0736+01	0.19	16.47	-23.47	8.1	S(Kim)	-24.12	-23.39	-23.39	0.381	R	3600	27.52	1.48	D	N
PKS 1020-103	0.2	16.11	-24.17	8.7	S(Kim)	-23.38	-23.02	-23.02	0.061	R	3600	27.20	1.19	D	I
PKS 1217+02	0.24	15.97	-24.77	8.3	S(Kim)	-24.28	-23.4	-23.4	0.278	R	3600	27.02	0.74	D	N
PKS 2135-14	0.2	15.53	-24.87	8.9	S(Kim)	-23.98	-23.12	-23.12	0.043	R	4440	26.48	1.57	D	N
PKS 2349-01	0.17	16.59	-23.27	8.6	S(Kim)	-23.81	-23.34	-23.75	0.12	R	3080	27.25	0.84	D	T
PKS 2355-082	0.21	17.5	-23.07	8.6	S(Kim)	-23.02	-23.32	-23.5	0.034	R	4680	26.85	0.94	D	T

Note. — Column 1: object name; column 2: redshift; column 3: apparent magnitude in the  $V$  band from Véron-Cetty & Véron (2010); column 4: absolute  $R$ -band magnitude, converted from absolute  $B$ -band magnitude; column 5: the black hole mass; column 6: references for  $M_{\text{BH}}$  and method for estimating  $M_{\text{BH}}$ : R=reverberation mapping; S=single-epoch method; Kim=Kim et al. (2008a); K15; V&P=Vestergaard & Peterson (2006); column 7: absolute  $R$ -band magnitude of the AGN nuclear component; column 8: absolute  $R$ -band magnitude of the bulge of the AGN; column 9: absolute  $R$ -band magnitude of the AGN host galaxy (see section 2.3 for how we derived quantities in columns 5 and 7–9). Bulge magnitudes come from an SB fitting of the images from D or C in the column 15 and from the black hole mass for Ma or Mc in the column 15; column 10: Eddington ratio from Kim et al. (2008a); column 11: filter; column 12: integrated exposure time; column 13: surface-brightness limit, averaged over a  $1'' \times 1''$  area at  $1\sigma$  per pixel in the observed band;

column 14: seeing FWHM in arcseconds; column 15: telescope: D=2.5m DuPont telescope in Las Campanas, C=CFHT, Ma=1.5m telescope in Maidanak observatory, Mc=2.1m telescope in McDonald observatory; column 16: merging type T=tidal tail; S=shell structures; I=interaction; N=no merging feature.

<sup>a</sup> Typical formal error is  $< 0.1$  dex, but the error arising from the intrinsic scatter of the  $M_{\text{BH}}$  estimators could be as much as 0.4 dex.

<sup>b</sup> Typical error is  $\sim 0.1$  mag.

<sup>c</sup> Typical error is  $\pm 0.3 - \pm 0.4$  mag.

<sup>d</sup> Typical error is  $\pm 0.2$ .

Table 2. Fitted Parameters

Name	$m_{\text{Nuc}}$ (mag)	$m_{\text{Bul}}$ (mag)	$R_e$ ( $''$ )	$n$	$m_{\text{disk}}$ (mag)	$R_d$ ( $''$ )	$n_d$	$\chi_v^2$	Filter
(1)	(2)	(3)	(4)	(5)	(6)	(7)	(8)	(9)	(10)
CTS J17.17	$16.74 \pm 0.00$	$16.24 \pm 0.01$	$2.2 \pm 0.01$	$1.27 \pm 0.02$	$16.4 \pm 0.01$	$6.23 \pm 0.16$	1	1.18	i
PKS 0159-062	$19.11 \pm 0.01$	$17.37 \pm 0.00$	$4.36 \pm 0.03$	[4]	-	-	-	1.11	r

Note. — column 1: object name of CFHT data fitted through GALFIT; column 2: apparent nuclear magnitude in the observed filter; column 3: apparent bulge magnitude in the observed filter; column 4: effective radius of the bulge; column 5: Sersic index of the bulge; column 6: apparent disk magnitude in the observed filter; column 7: disk scale length; column 8: sersic index of the disk; column 9: reduced  $\chi^2$ ; column 10: filter.



Table 3. Control Sample of Early-type Galaxies

Sequence (Number) (1)	SDSS ID (2)	R.A. (deg) (3)	Decl. (deg) (4)	$z$ (5)	$R$ (mag) (6)	Error (mag) (7)	$B/T$ (8)	Error (9)	$M_R$ (mag) (10)	Error (mag) (11)	$M_{\text{BH}}$ $\log(M/M_{\odot})$ (12)	Type Kaviraj (2010) (13)	Type This work (14)
2	587730845817504263	321.915192	-1.102175	0.030	14.739	0.003	0.150	0.000	-18.800	0.020	6.875	1	N
10	587730846891507736	322.370728	-0.219635	0.050	14.415	0.002	0.410	0.010	-21.320	0.020	8.135	4	T
13	587730846891507870	322.451935	-0.313562	0.030	14.518	0.002	0.550	0.000	-20.490	0.010	7.720	3	N
24	587730847963939362	319.503601	0.570868	0.035	15.062	0.003	0.940	0.020	-20.980	0.020	7.965	1	N
49	587730848501596412	321.287964	0.896778	0.049	15.267	0.003	0.490	0.010	-20.660	0.010	7.805	1	N
50	587730848501399575	320.744537	1.026719	0.031	14.173	0.002	0.500	0.010	-20.630	0.010	7.790	1	N
76	587731174382567703	320.190460	0.790999	0.043	15.405	0.003	0.990	0.010	-21.080	0.010	8.015	1	N
89	587731185116053719	327.825348	-0.957031	0.027	13.665	0.002	1.000	-99.990	-21.584	0.002	8.267	2	T
112	587731185125818492	350.121124	-1.002414	0.031	13.519	0.002	1.000	-99.990	-22.015	0.002	8.483	1	N
128	587731185650565143	322.302155	-0.621743	0.030	14.433	0.002	0.520	0.000	-20.360	0.010	7.655	2	T
129	587731185650565167	322.305756	-0.523884	0.030	14.723	0.003	0.530	0.000	-20.060	0.010	7.505	1	N
135	587731185651155402	323.751648	-0.511436	0.030	14.439	0.002	0.500	0.000	-20.270	0.010	7.610	2	T
146	587731185654366563	331.085999	-0.502819	0.046	15.855	0.004	0.340	0.010	-19.310	0.040	7.130	1	N
192	587730846893080588	325.963776	-0.321398	0.027	14.169	0.002	0.570	0.010	-20.400	0.010	7.675	1	N
221	587731186724110554	321.939697	0.326403	0.031	14.692	0.003	0.750	0.010	-20.540	0.020	7.745	1	N
237	587731186735186207	347.261871	0.266889	0.033	15.056	0.003	0.560	0.010	-19.680	0.020	7.315	2	T
261	587731187271663782	346.281830	0.826253	0.042	15.627	0.003	0.960	0.060	-20.980	0.070	7.965	2	T
266	587731187279069315	3.300832	0.742940	0.039	14.342	0.002	0.880	0.010	-21.640	0.010	8.295	1	N
269	587731187279593490	4.393614	0.743043	0.044	14.596	0.002	0.880	0.010	-21.790	0.010	8.370	2	T
272	587731187279462423	4.088767	0.788624	0.044	15.253	0.003	0.700	0.010	-20.790	0.010	7.870	1	N

Note. — column 1: sequence number of Kaviraj (2010); column 2: SDSS object ID; column 3: R.A. (J2000); column 4: Decl. (J2000); column 5: redshift; column 6-7: apparent  $R$ -band magnitude and its error; column 8-9:  $B/T$  and its error. The error of -99.990 indicates that the SB model does not have a disk component; column 10-11: absolute  $R$ -band magnitude of the bulge component and its error; column 12: black hole mass; column 13: morphological classification from Kaviraj (2010): 1:relaxed, 2:tidal feature, 3:dust feature, 4:tidal and dust feature, 5:interacting, 7:spheroids with faint disk; column 14: morphological classification from this work: N:relaxed, T:tidal feature, S:shell-type. (This table is available in its entirety in a machine-readable form in the online journal. A portion is shown here for guidance regarding its form and content.)

Table 4. Merging Fraction of Simulated AGNs I

	$\log(M_{\text{BH}}/M_{\odot}) < 8.39$					$\log(M_{\text{BH}}/M_{\odot}) \geq 8.39$				
	Redshift									
$m_{\text{Nuc}}$	0.041	0.086	0.138	0.2	0.275	0.041	0.086	0.138	0.2	0.275
None	0.141	0.116	0.074	0.0141	0.011	0.455	0.394	0.303	0.091	0.061
$m_{\text{gal}}$	0.137	0.106	0.067	0.014	0.007	0.424	0.364	0.242	0.091	0.061
$m_{\text{gal}} - 1.0$	0.127	0.095	0.042	0.004	0.004	0.394	0.303	0.212	0.061	0.030
$m_{\text{gal}} - 1.5$	0.123	0.085	0.042	0.004	0.004	0.364	0.242	0.212	0.061	0.030

Note. — The simulated AGNs are divided into two  $M_{\text{BH}}$  bins, and the results are for the seeing of  $1''$ . They are simulated to be at several different redshifts and to have various nuclear magnitudes.

Table 5. Merging Fraction of Simulated AGNs II

	$1''$					$2''$				
	Redshift									
$m_{\text{Nuc}}$	0.041	0.086	0.138	0.2	0.275	0.041	0.086	0.138	0.2	0.275
None	0.167	0.142	0.098	0.022	0.016	0.164	0.132	0.069	0.009	0.003
$m_{\text{gal}}$	0.167	0.132	0.085	0.022	0.013	0.155	0.12	0.057	0.009	0.003
$m_{\text{gal}} - 1.0$	0.151	0.11	0.06	0.009	0.006	0.145	0.085	0.041	0.003	0.00
$m_{\text{gal}} - 1.5$	0.151	0.11	0.06	0.009	0.006	0.145	0.085	0.038	0.003	0.00

Note. — The results for two seeing conditions ( $1''$  and  $2''$ ) are presented for simulated AGNs placed at several different redshifts and with different nuclear magnitudes.

Table 6. Merging Fraction of AGNs versus Simulated AGNs

$\log(M_{\text{BH}}/M_{\odot})$	AGN		Simulated AGN
	Base	Best ( $M_{\text{Nuc}}(R) < -22.44$ )	$m_{\text{PSF}} = m_{\text{gal}} - 1$ $1''$ seeing
$7.3 < \log(M_{\text{BH}}/M_{\odot}) < 8.39$	$0.389^{+0.121}_{-0.098}$	$0.333^{+0.135}_{-0.096}$	$0.051^{+0.017}_{-0.010}$
$8.39 \leq \log(M_{\text{BH}}/M_{\odot}) < 9.0$	$0.476^{+0.106}_{-0.102}$	$0.444^{+0.117}_{-0.106}$	$0.117^{+0.083}_{-0.036}$

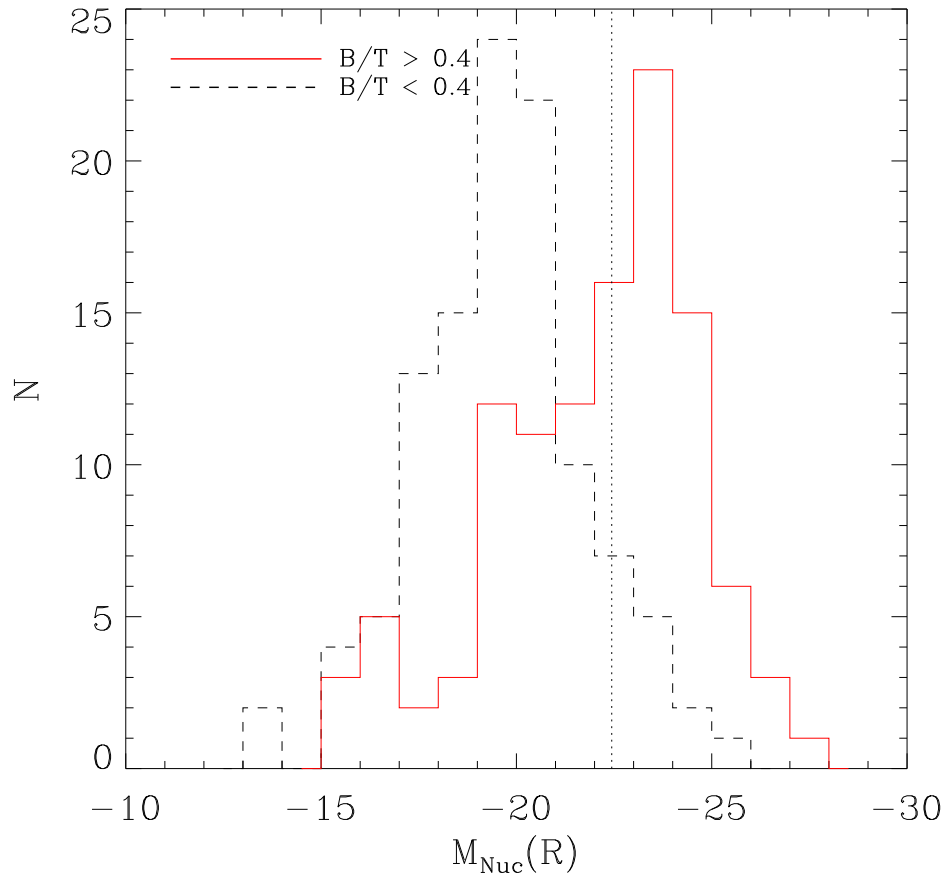


Fig. 1.— Distribution of AGN nuclear magnitude in the  $R$ band from K15. The red solid line shows the nuclear magnitude distribution of AGNs for which the host galaxy has  $B/T \geq 0.4$ . The black dashed line shows the nuclear magnitude distribution of AGNs for which the host galaxy has  $B/T < 0.4$ . The black dotted line represents a cut at  $M_{\text{Nuc}} = -22.44$  mag. This figure shows that the host galaxies of AGNs with  $M_{\text{Nuc}}(R) < -22.44$  mag are mostly bulge-dominated galaxies.

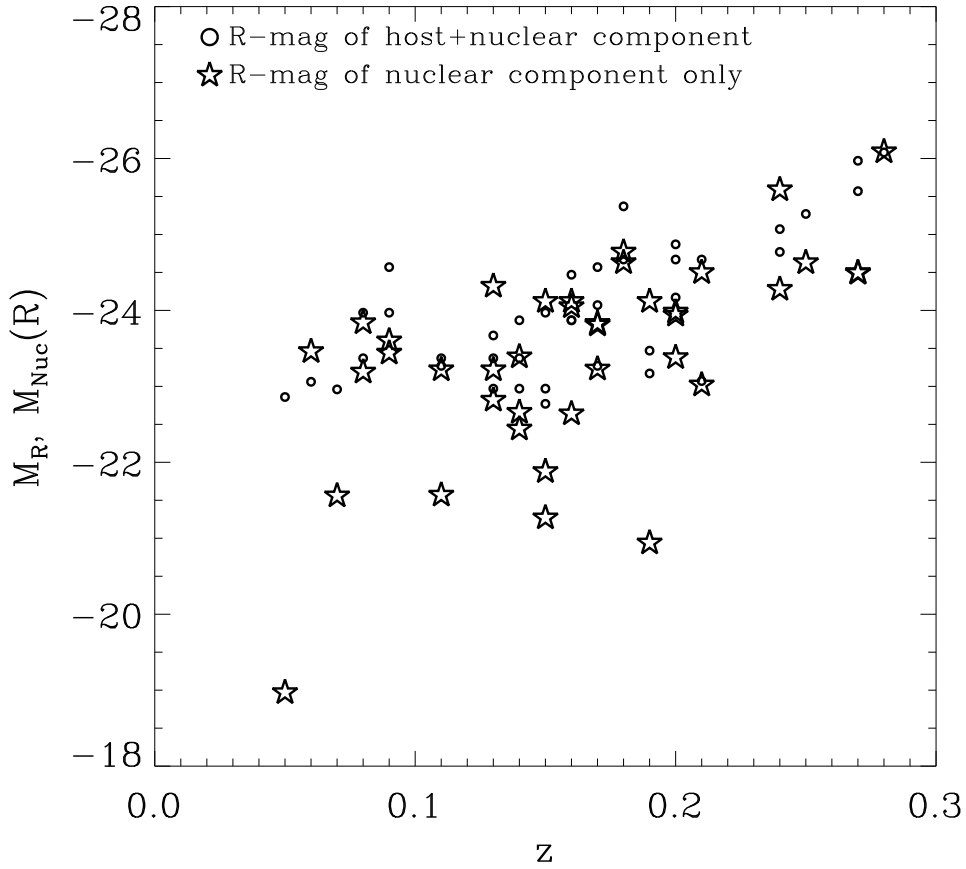


Fig. 2.— Redshift versus absolute magnitude in the  $R$  band of the host + nuclear component (small circles) and the nuclear component only ( $M_{\text{Nuc}}(R)$ ; stars) for 39 AGNs. See section 2.3 for how we derived  $M_{\text{Nuc}}$ .

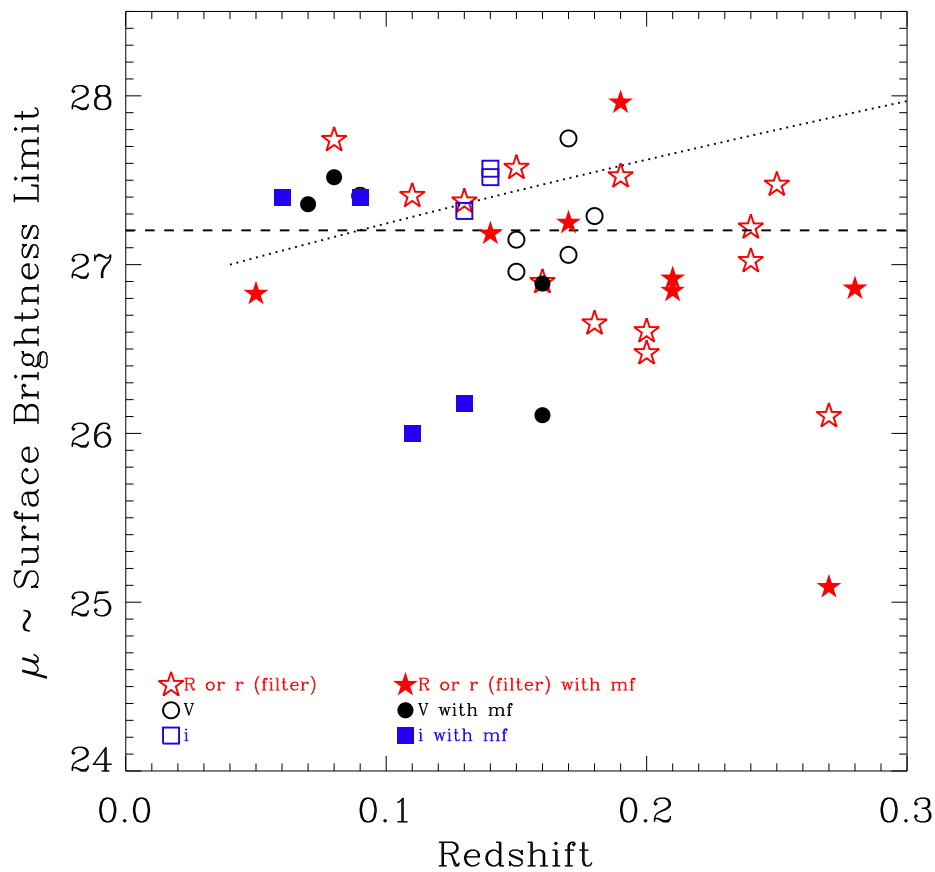


Fig. 3.— Redshift versus observed surface-brightness limits of 39 AGNs. The black dashed line is the median limit,  $27.2 \text{ mag arcsec}^{-2}$  at  $1\sigma$ . The red stars, the black circles, and the blue squares are the surface-brightness limits in the  $R$  or  $r$ ,  $V$ , and  $i$  filters, respectively. The filled symbols denote AGNs that have merging features (see Section 4). The dotted line indicates the effective surface brightness limit of the control sample images (See Section 3.2).

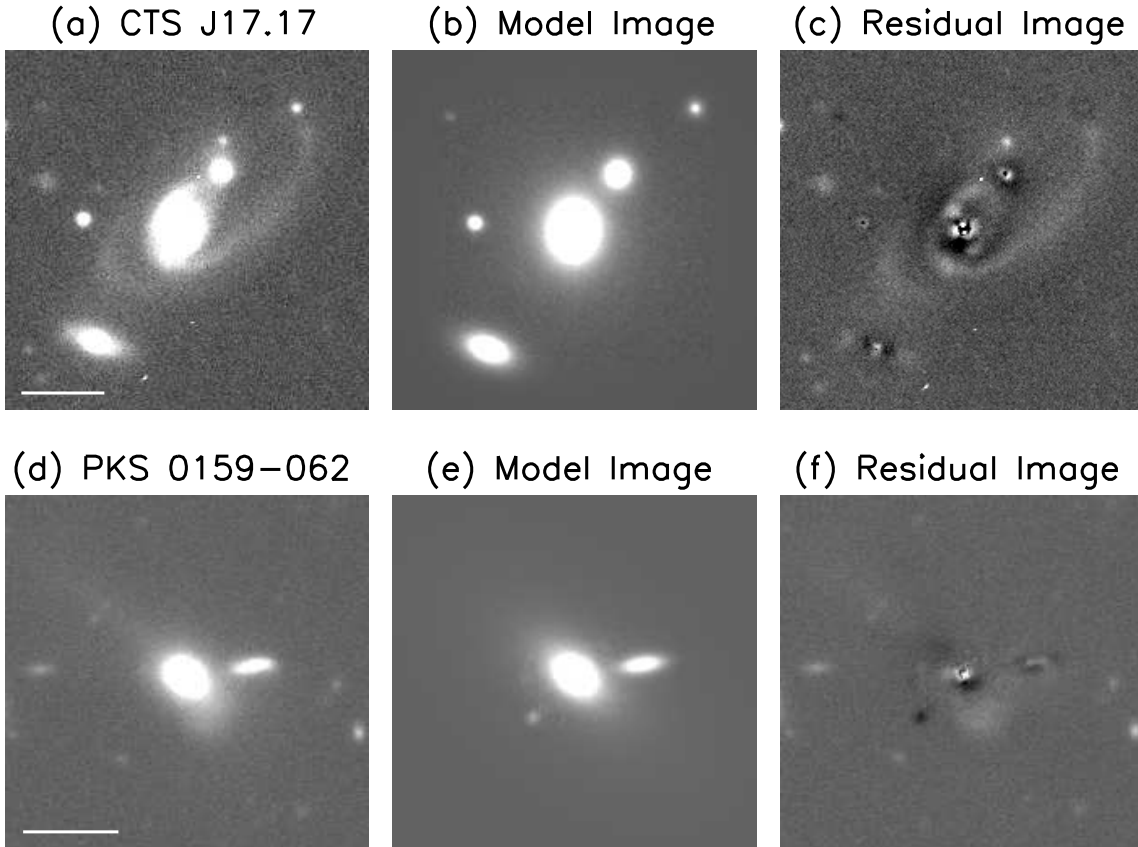


Fig. 4.— CFHT images of two AGNs fitted by GALFIT: (a) original, (b) model, and (c) residual images of CTS J17.17, and (d) original, (e) model, and (f) residual images of PKS 0159-062. The length of the horizontal bar in each panel is  $10''$ . The background of each image is subtracted, and the pixel values are square-rooted to bring out the low surface-brightness features. Identical pixel value scales are adopted to plot images for the same object.

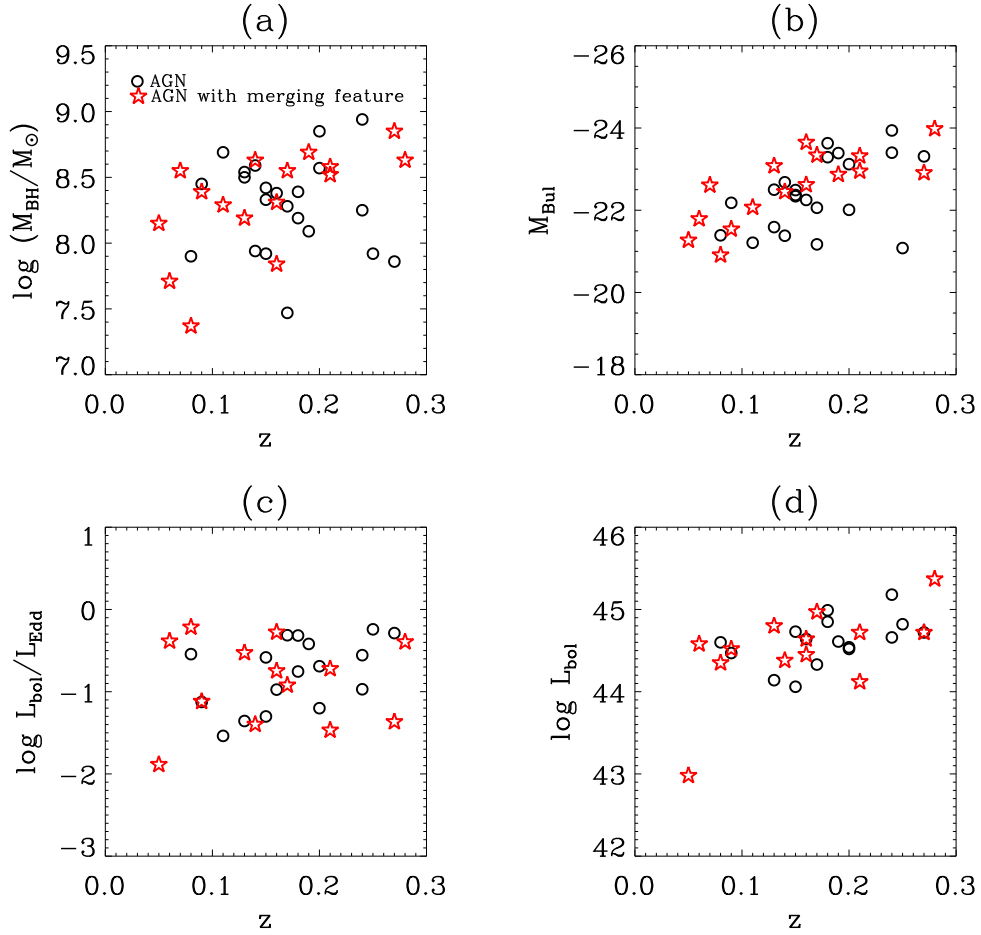


Fig. 5.— Redshift versus (a) BH masses, (b) the host bulge magnitudes, (c) the Eddington ratios, and (d) the bolometric luminosities of the base AGN sample (black circles) and AGNs with a merging feature as classified in Section 4 (red stars).

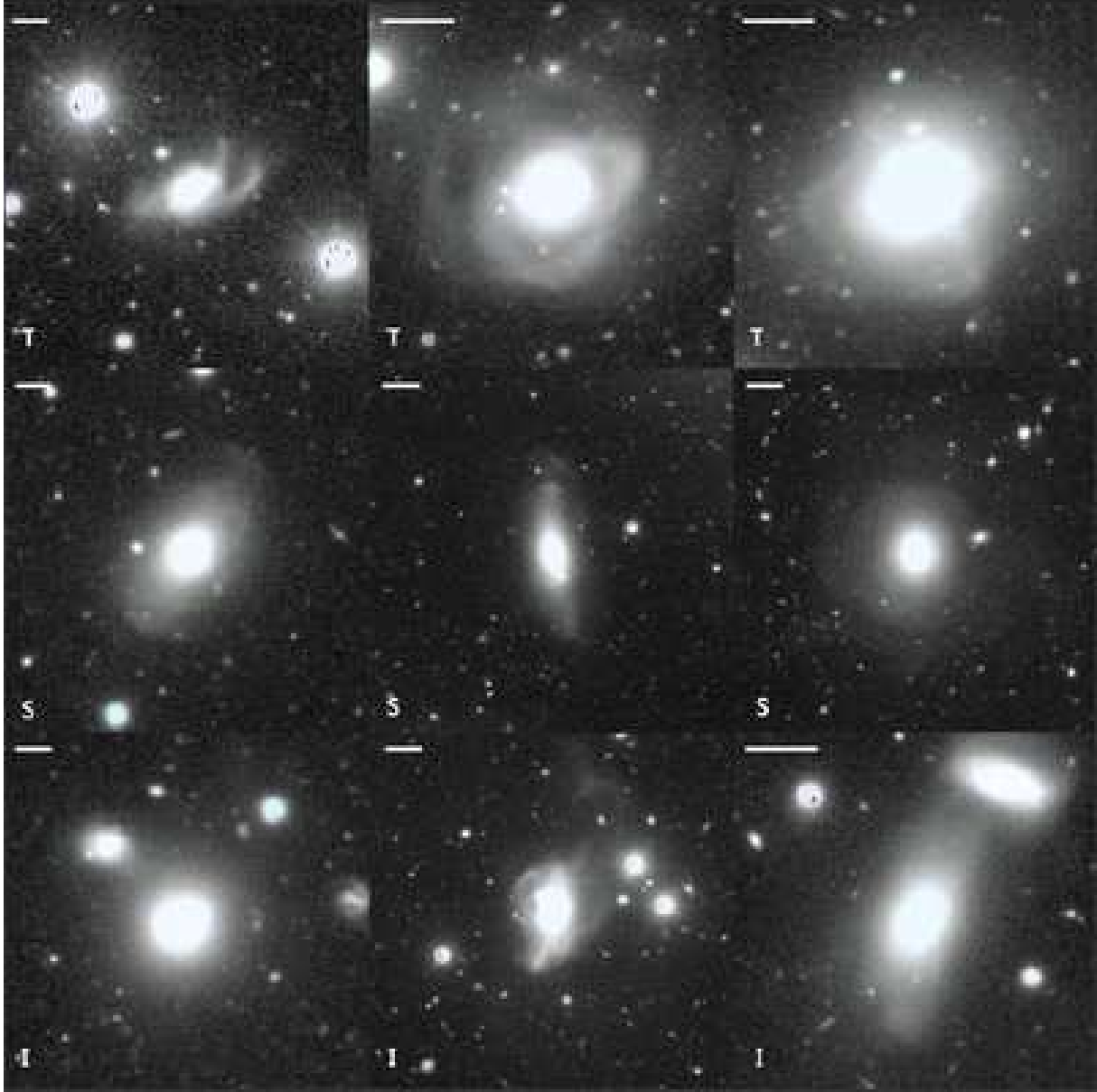


Fig. 6.— Examples of the Stripe 82 early-type galaxies with merging features classified as tidal tail (T), shell (S), interaction (I) types, respectively. The length of the horizontal bar in each panel is  $10''$ .



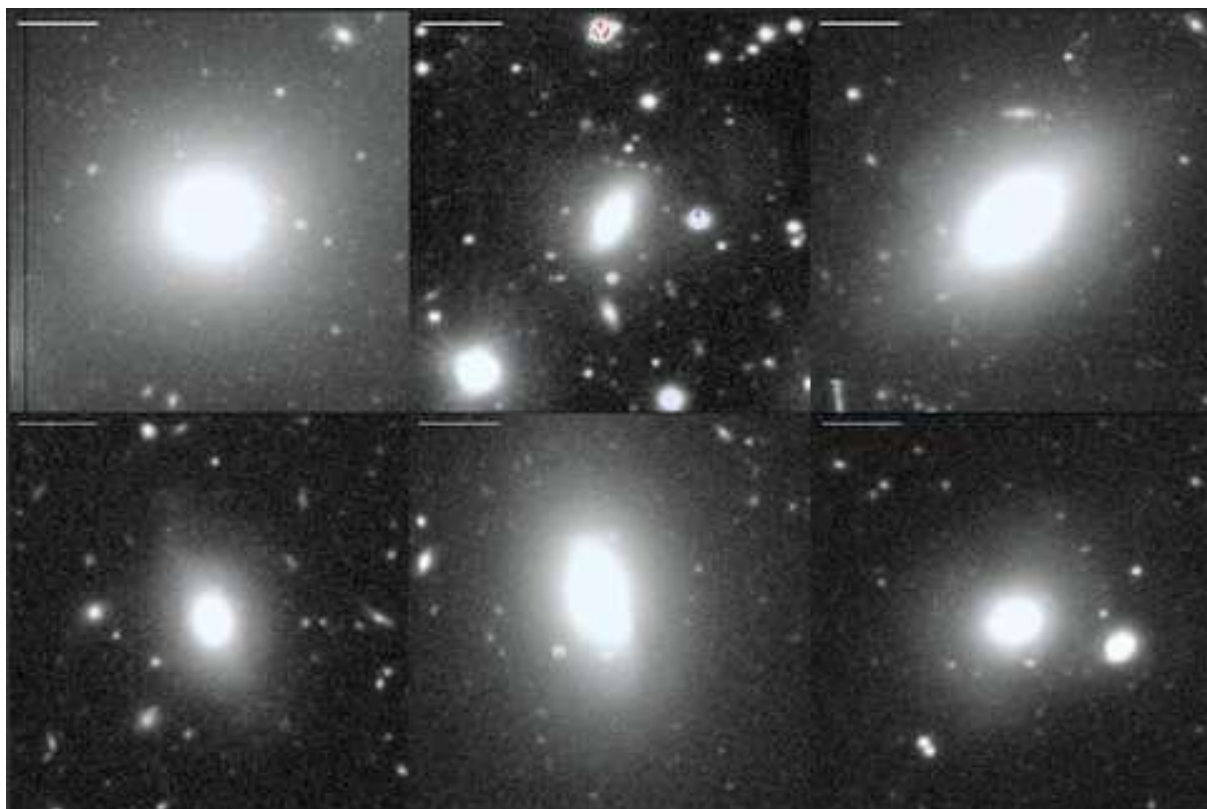


Fig. 7.— Examples of galaxies with ambiguous classification. They are classified as merging systems by Kaviraj (2010). However, we do not identify the merging feature, and it is likely that the merging feature, even if one assumes that it exists, will not be identified as such by us in our AGN sample. The length of the horizontal bar in each panel is  $10''$ .

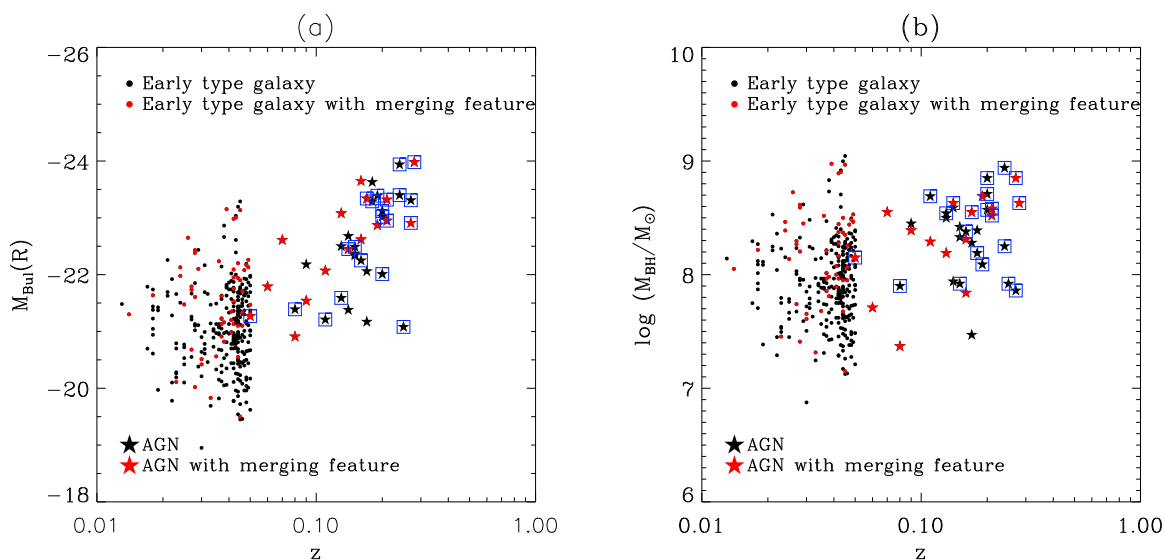


Fig. 8.— (a) Bulge magnitudes in the  $R$  band of the control sample early-type galaxies (small black circles), the control sample early-type galaxies with a merging feature (small red circles), AGN hosts (black stars), and AGN hosts with a merging feature (red stars) as a function of redshift, (b) Black hole masses of the control sample early-type galaxies (black circles), the control sample early-type galaxies with a merging feature (red circles), AGN hosts without (black stars) and with (red stars) merging feature as a function of redshift. The blue rectangles denote AGNs from the DuPont sample.

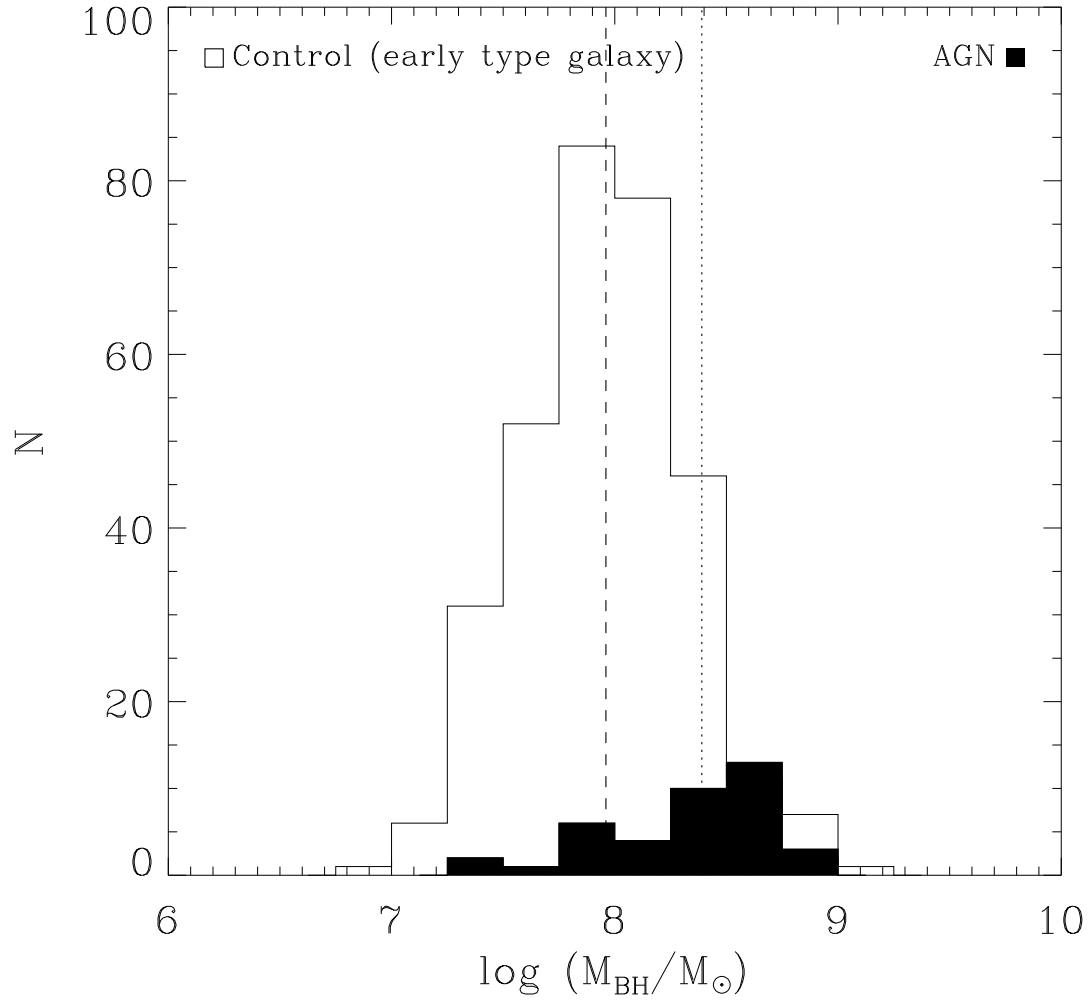


Fig. 9.— Black hole mass distribution of the control sample early-type galaxies and AGNs. The unfilled black histogram and the dashed line are the black hole mass distribution and its median ( $10^{7.96}M_{\odot}$ ) of the control sample early-type galaxies. The black filled histogram and the dotted line are the black hole mass distribution and its median ( $10^{8.39}M_{\odot}$ ) of the AGNs.

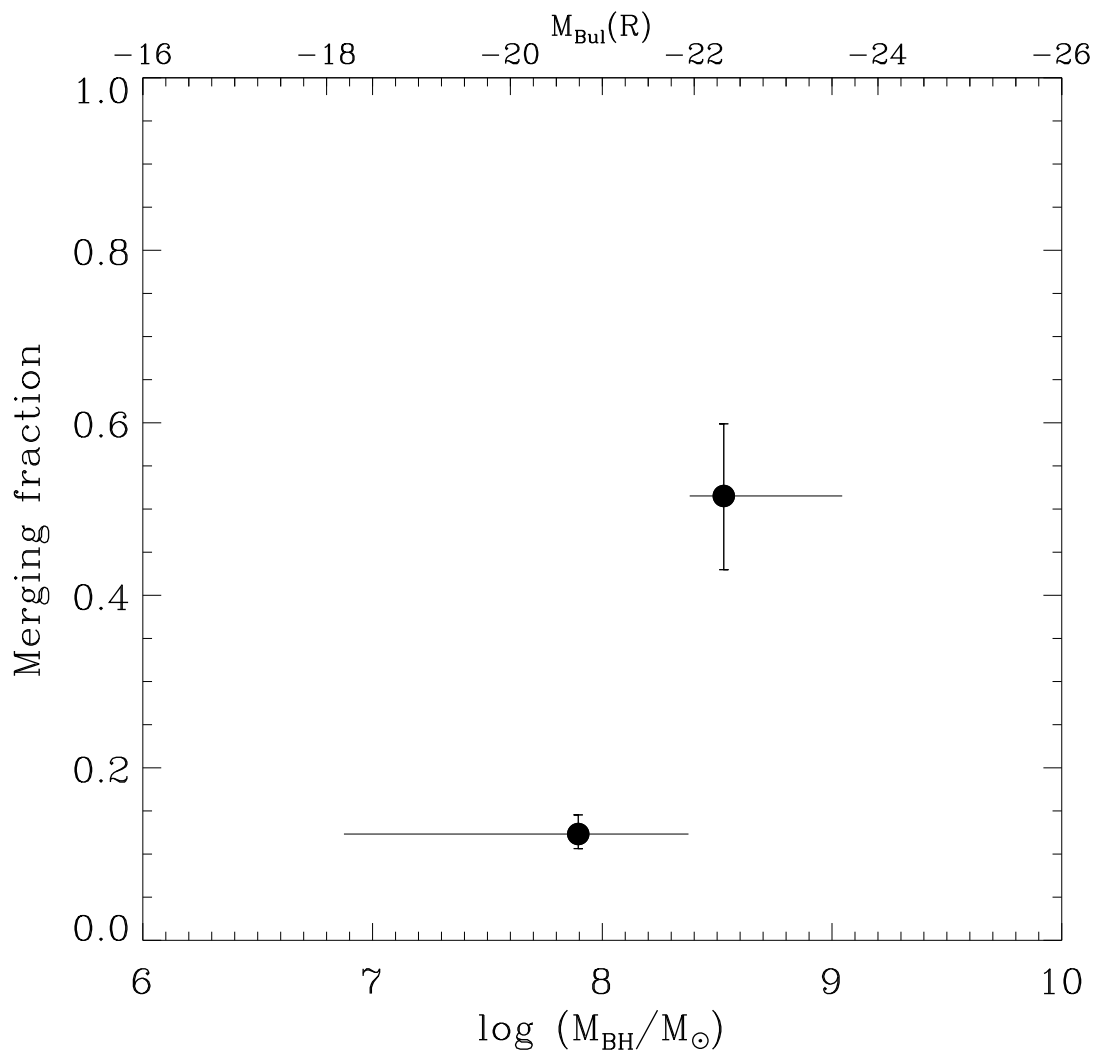


Fig. 10.— Merging fraction of the control sample early-type galaxies as a function of  $M_{\text{BH}}$  and  $M_{\text{Bul}}$ . The merging fraction increases as  $M_{\text{BH}}$  and  $M_{\text{Bul}}$  increases. The horizontal bars show the  $M_{\text{BH}}$  and  $M_{\text{Bul}}$  ranges covered by early-type galaxies in two bins divided at  $10^{8.39} M_{\odot}$  and -21.81 mag.

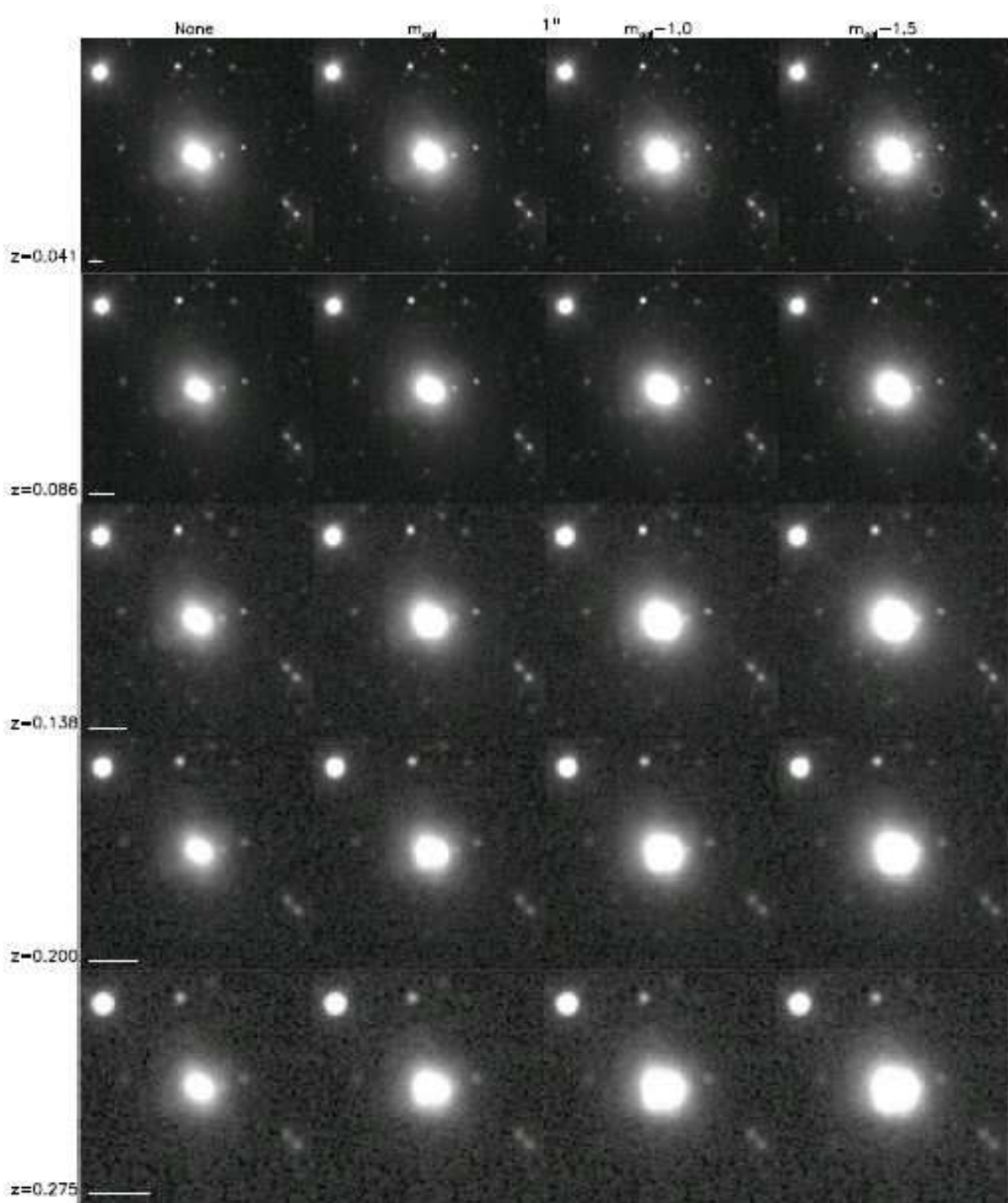


Fig. 11.— Examples of simulated AGN images. The seeing is  $1''$ . The redshifts and the magnitudes of the nuclear point sources are varied as indicated (see text). The length of the horizontal bar in each panel is  $10''$ .

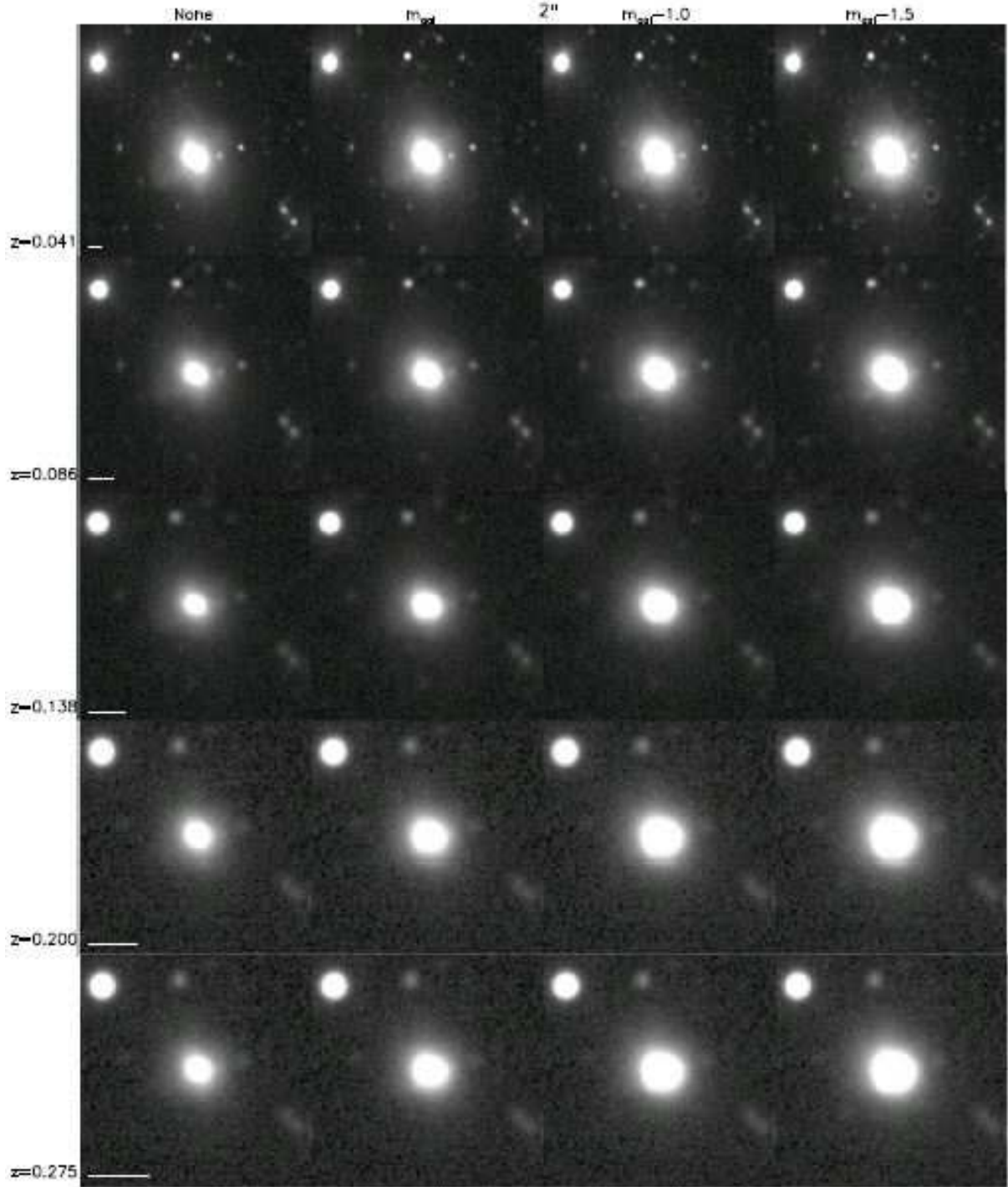


Fig. 12.— Examples of simulated AGN images. The seeing is  $2''$ . The redshifts and the magnitudes of the nuclear point sources are varied as indicated (see text). The length of the horizontal bar in each panel is  $10''$ .

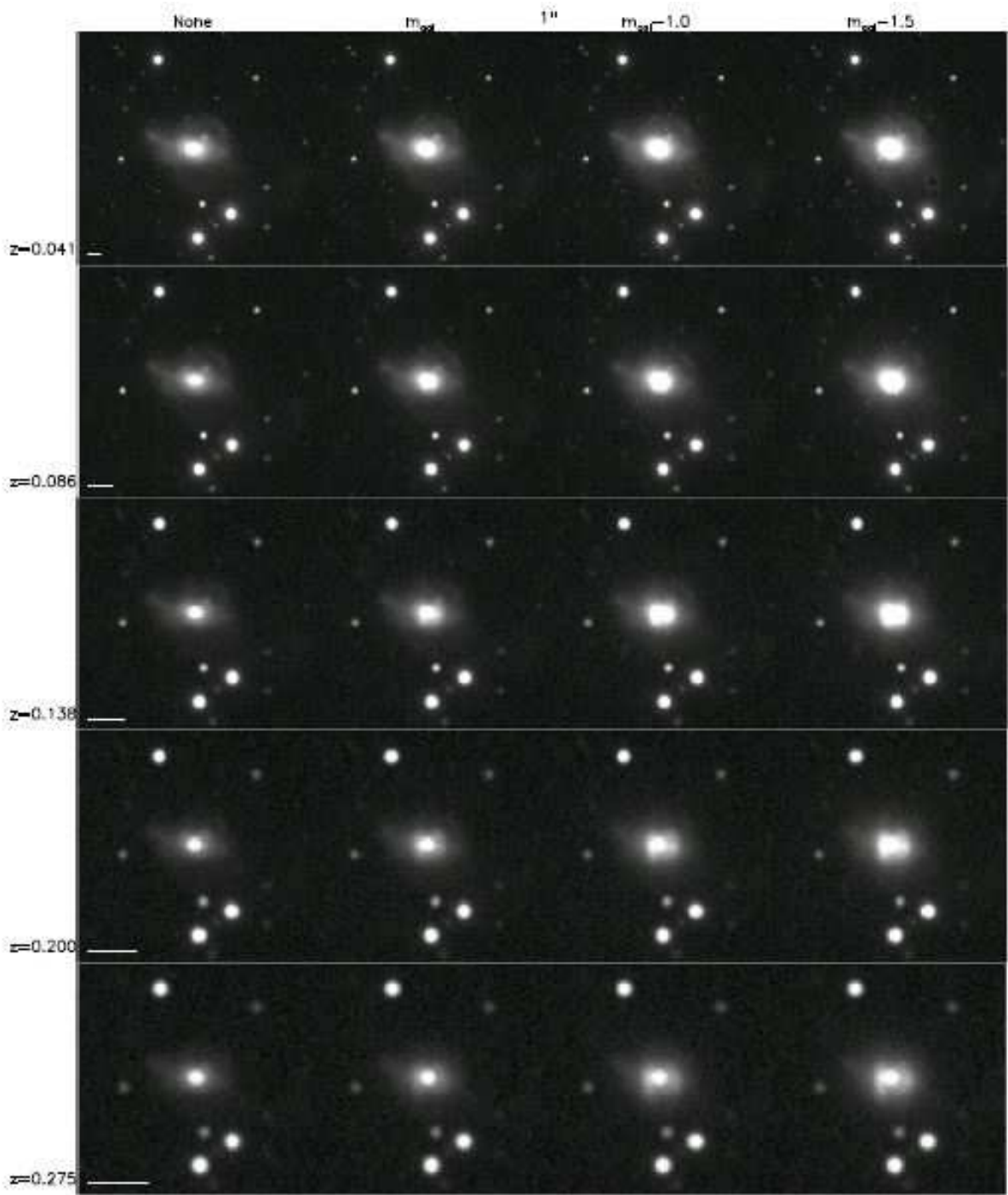


Fig. 13.— Examples of simulated AGN images. The seeing is  $1''$ . The redshifts and the magnitudes of the nuclear point sources are varied as indicated (see text). The length of the horizontal bar in each panel is  $10''$ .

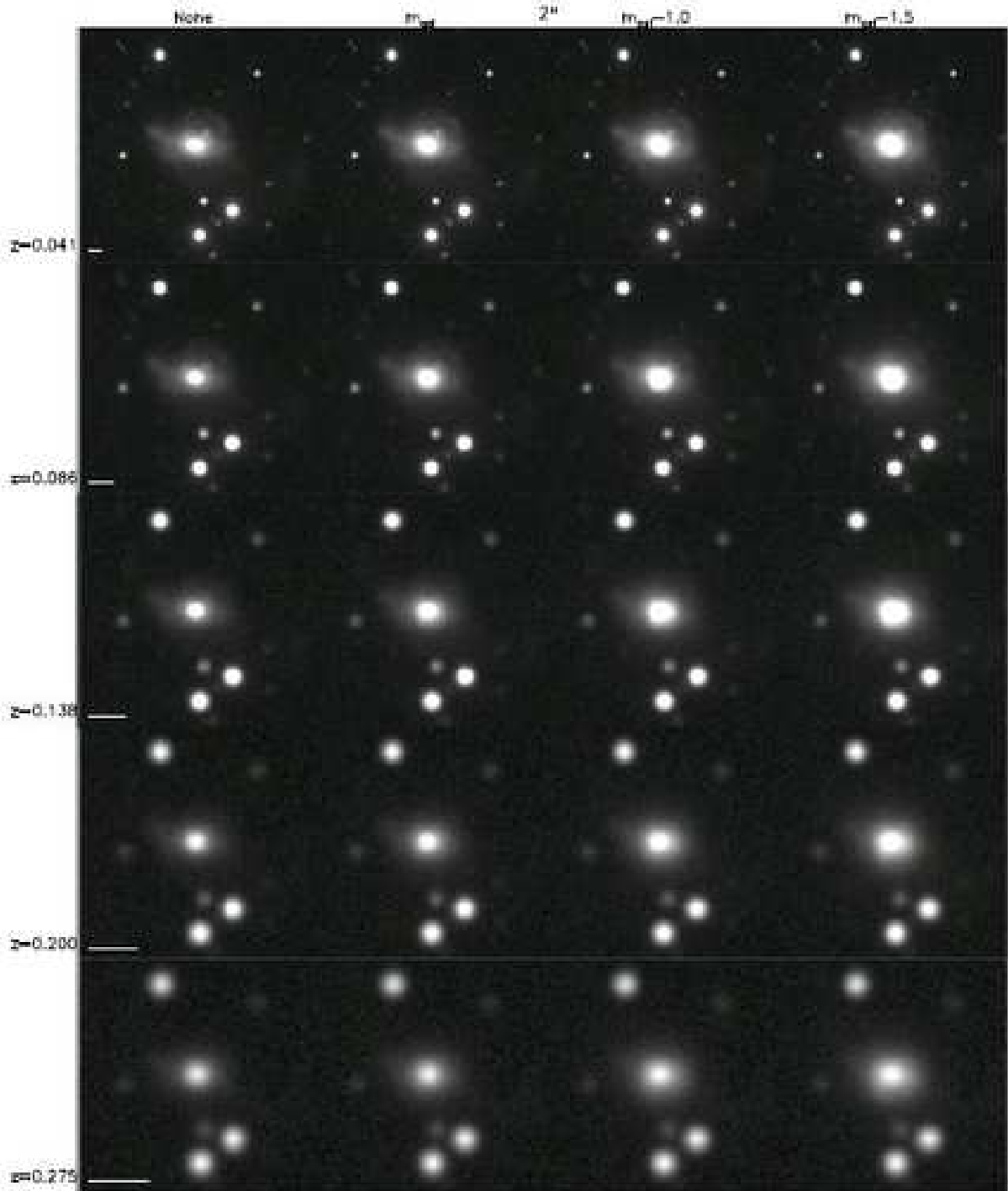


Fig. 14.— Examples of simulated AGN images. The seeing is  $2''$ . The redshifts and the magnitudes of the nuclear point sources are varied as indicated (see text). The length of the horizontal bar in each panel is  $10''$ .



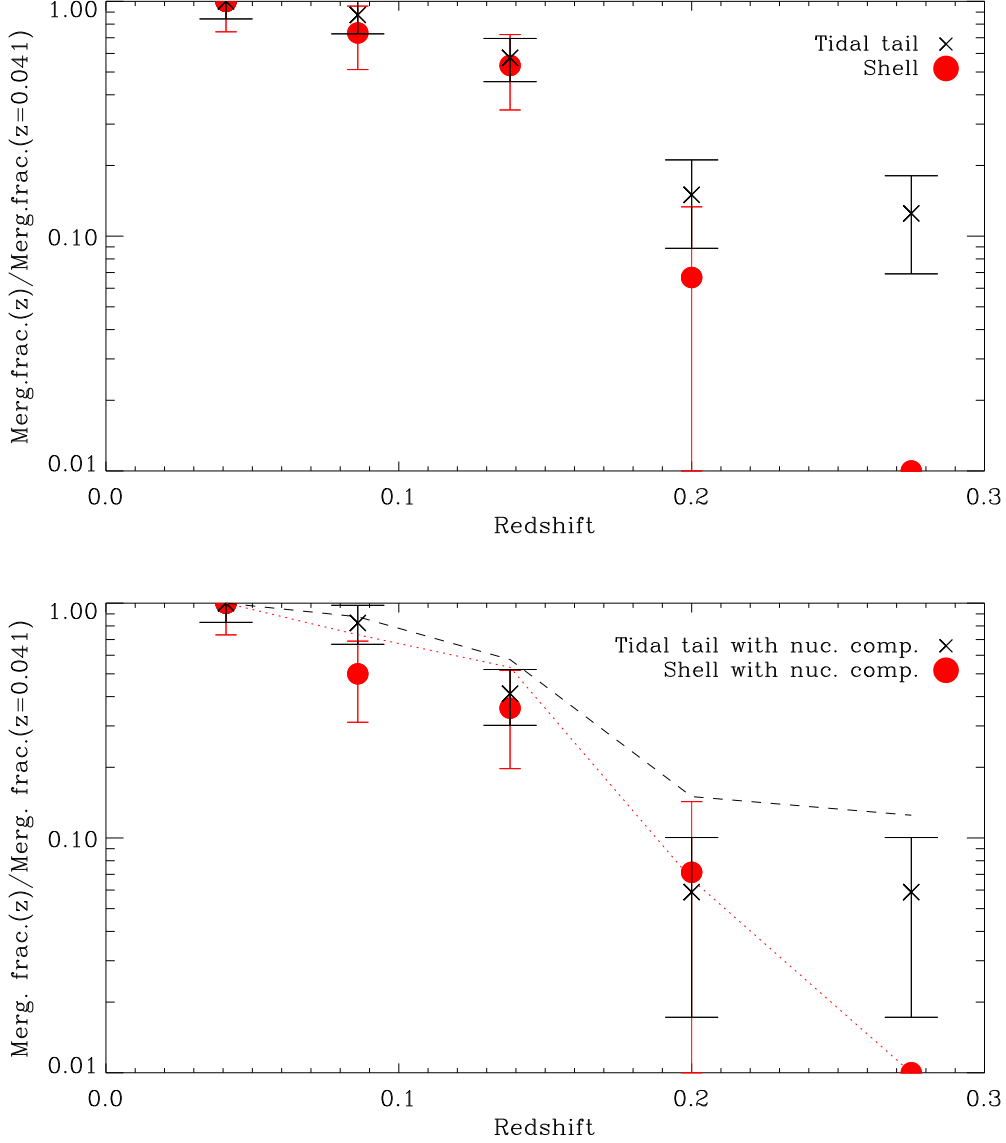


Fig. 15.— Change in the merging fraction when simulated AGNs are redshifted from  $z = 0.041$  to a higher redshift but without adding a nuclear component (the upper panel) and when the simulated AGNs are redshifted and a nuclear component is added (the bottom panel). The magnitude of the nuclear component is assumed to be  $m_{\text{Nuc}} = m_{\text{host}} - 1.0$  mag. Cases for two types of merging features (black cross for T type and red filled circles for S type) are indicated. The dashed and the dotted lines in the bottom figure denote the result for the T type and the S type in the upper figure, respectively.

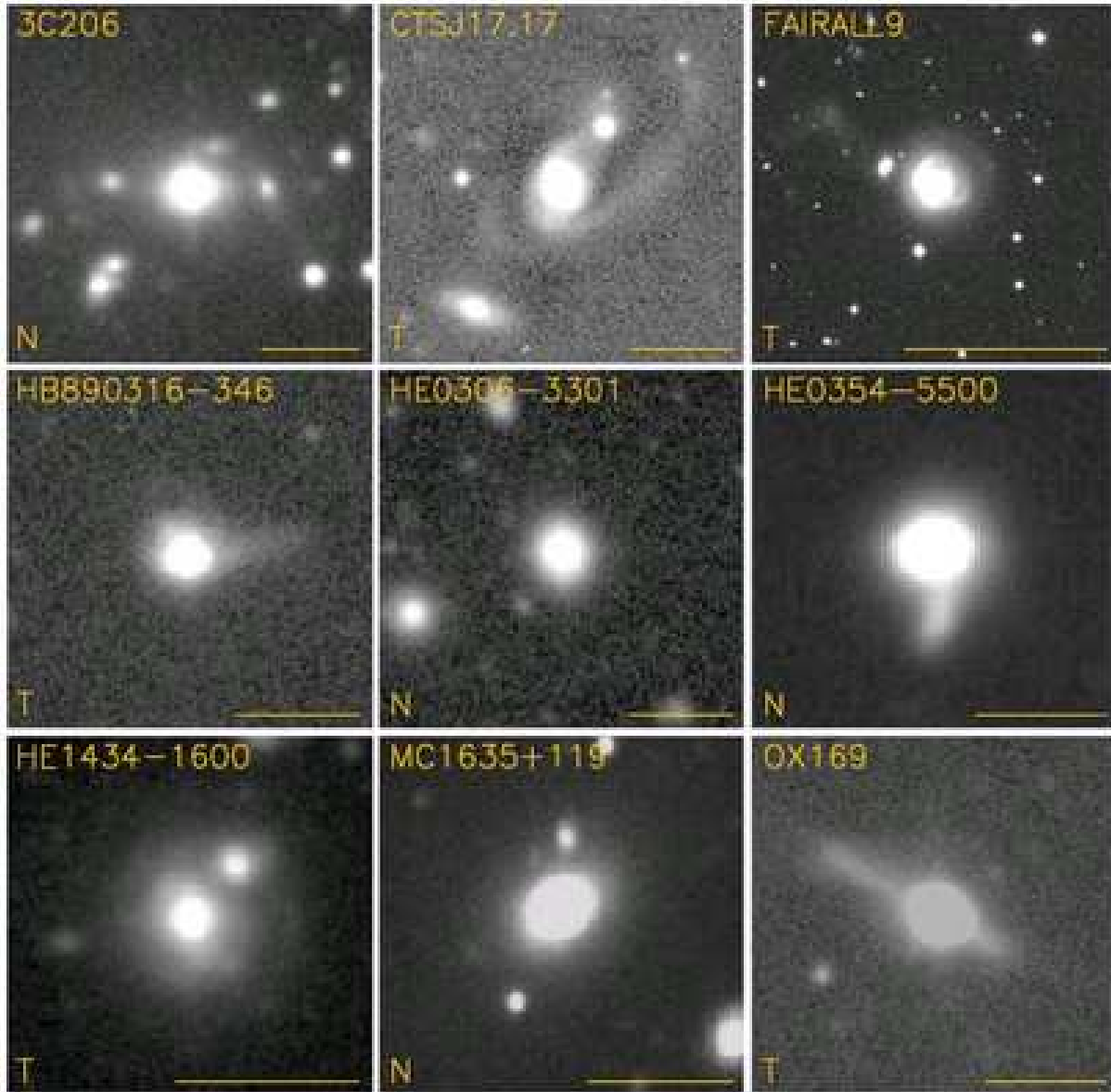


Fig. 16.— Images of 39 AGNs in our base sample. T=tidal-tail type, S=shell type, I=Interaction type. The length of horizontal bar in each panel is  $10''$ .

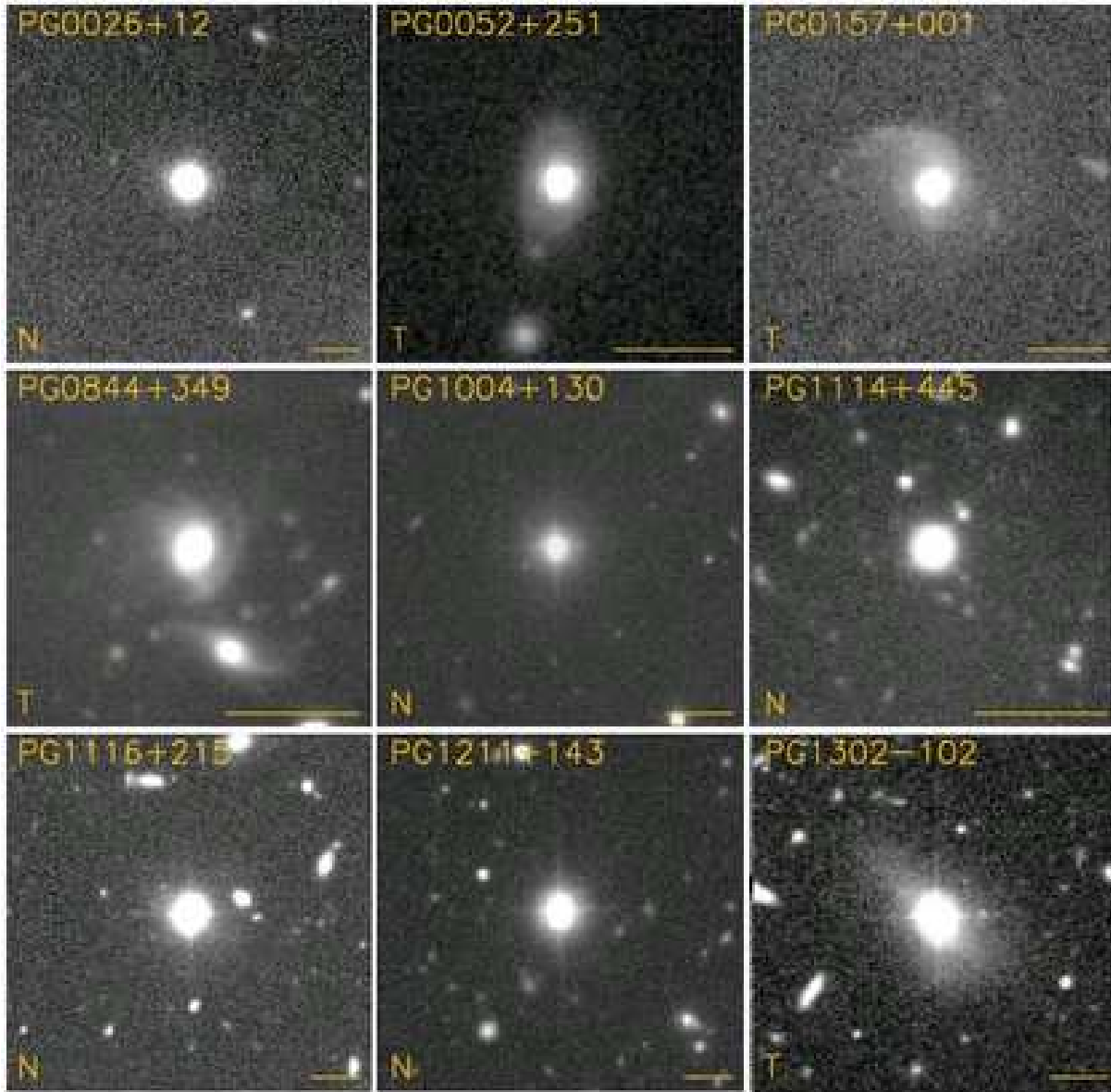


Fig. 16.— Continued

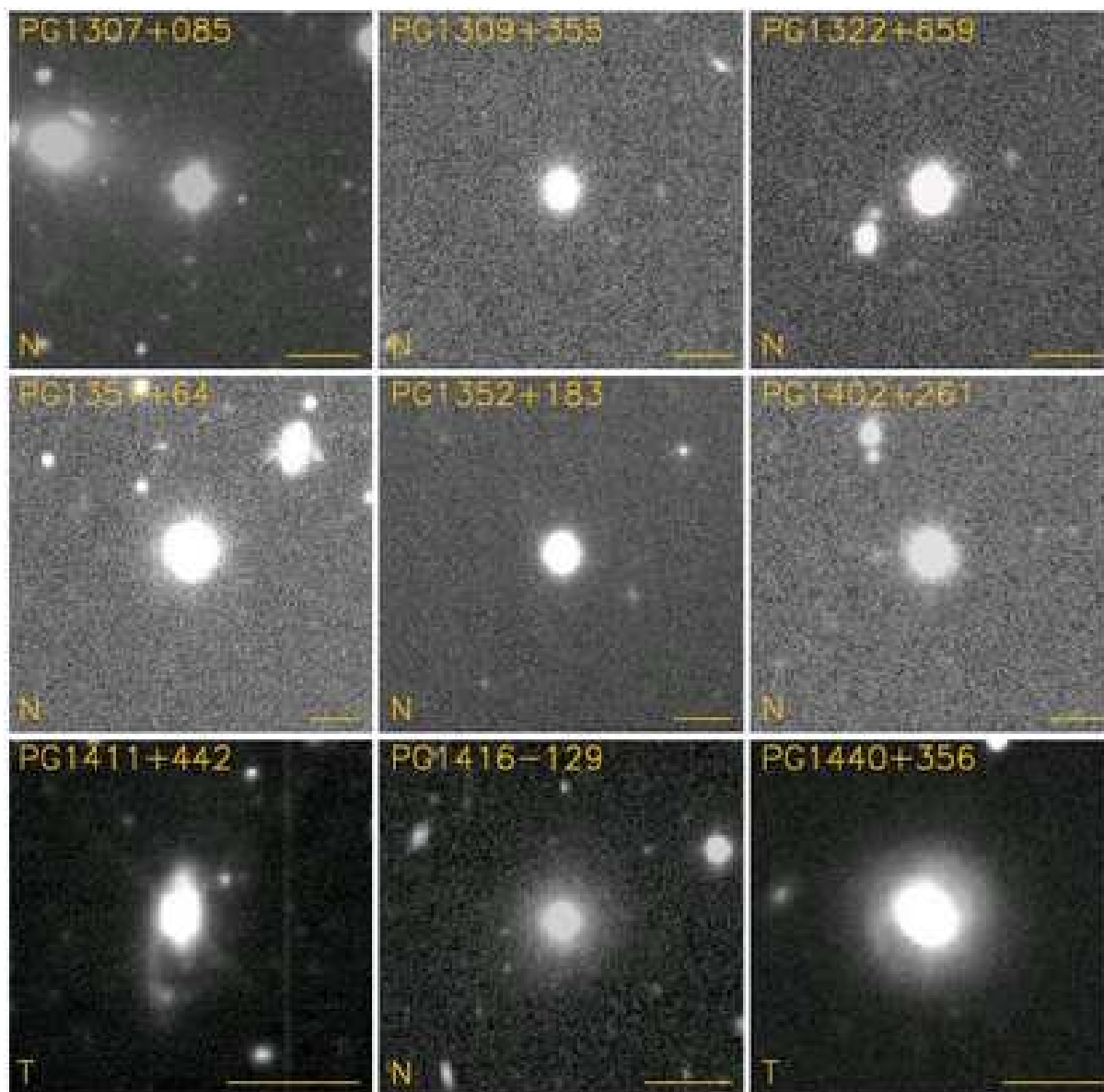


Fig. 16.— Continued

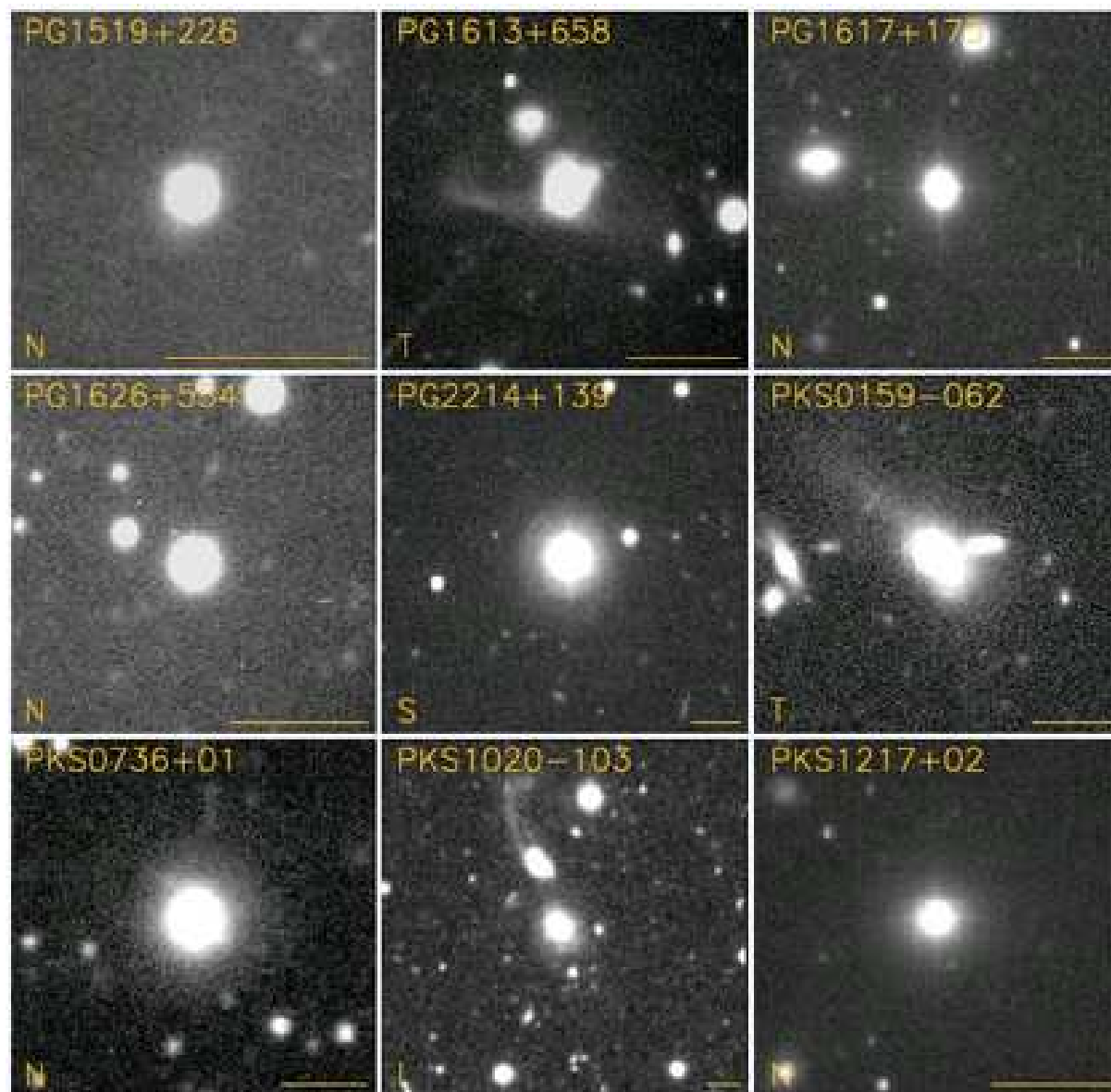


Fig. 16.— Continued

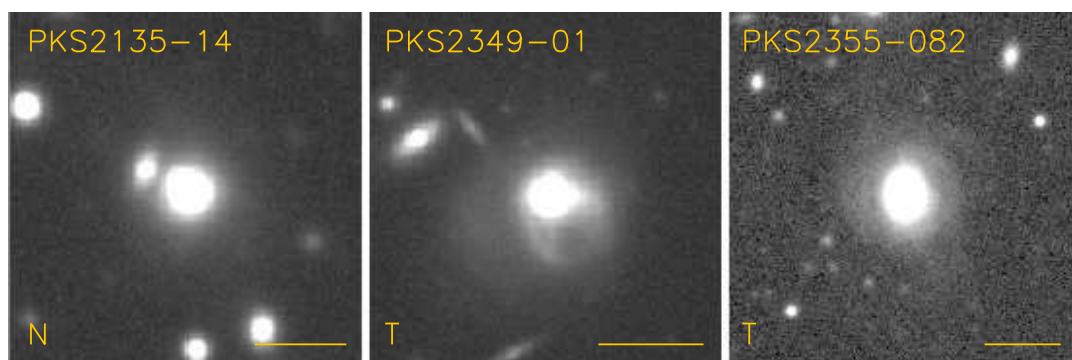


Fig. 16.— Continued

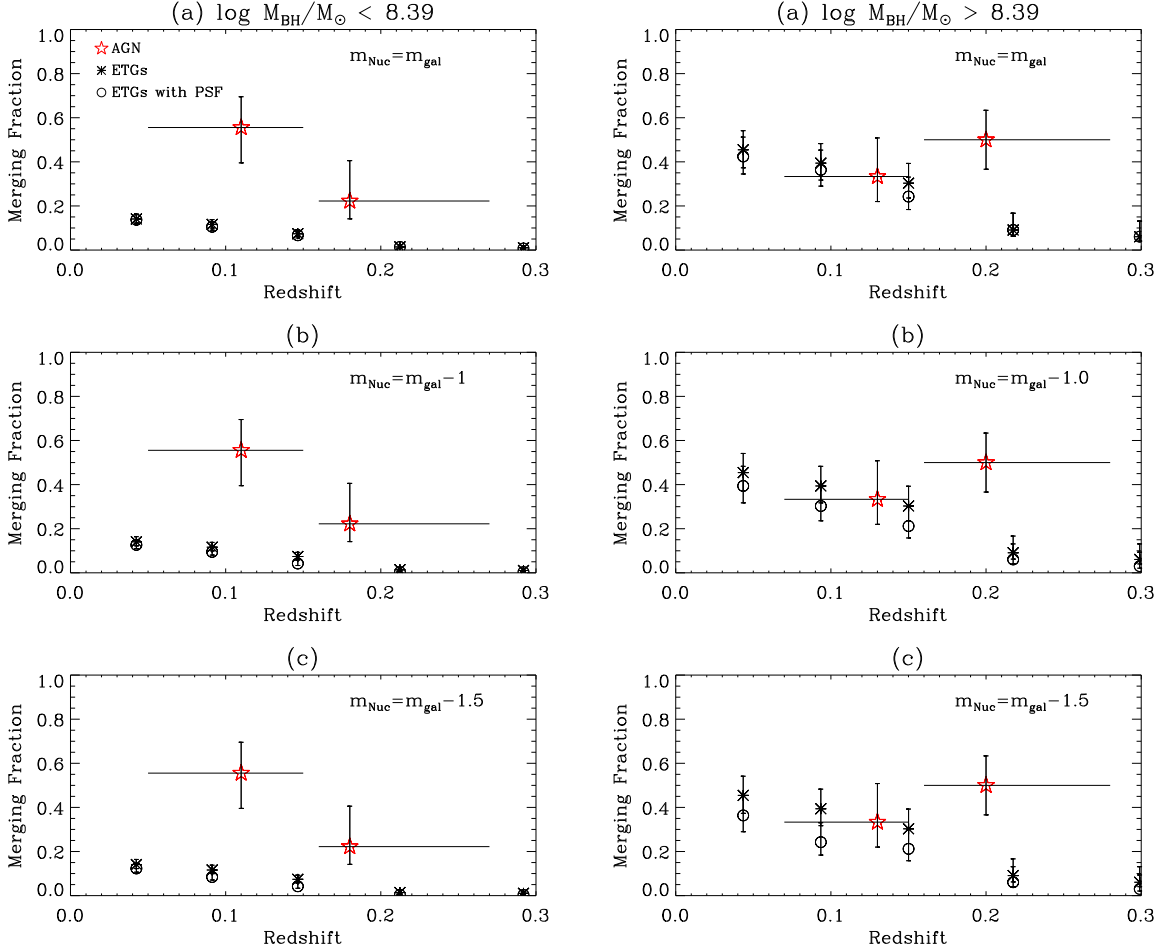


Fig. 17.— Merging fraction of AGNs and the simulated AGNs as a function of redshift. The left panel is the merging fraction of objects with  $\log(M_{\text{BH}}/M_{\odot}) < 8.39$ , and the right panel is the merging fraction of objects with  $\log(M_{\text{BH}}/M_{\odot}) \geq 8.39$ . The panels for each  $M_{\text{BH}}$  are also divided into three, each corresponding to a different nuclear magnitude. The magnitudes of the added PSF components for each panel are (a) top:  $m_{\text{gal}}$ , (b) middle:  $m_{\text{gal}} - 1.0$ , and (c) bottom:  $m_{\text{gal}} - 1.5$ . The black asterisks are the merging fraction of early-type galaxies without any nuclear source (PSF) included, and the black circles are the numbers for the cases with a nuclear component included. The seeing of simulated images is assumed to be  $1''$  here.

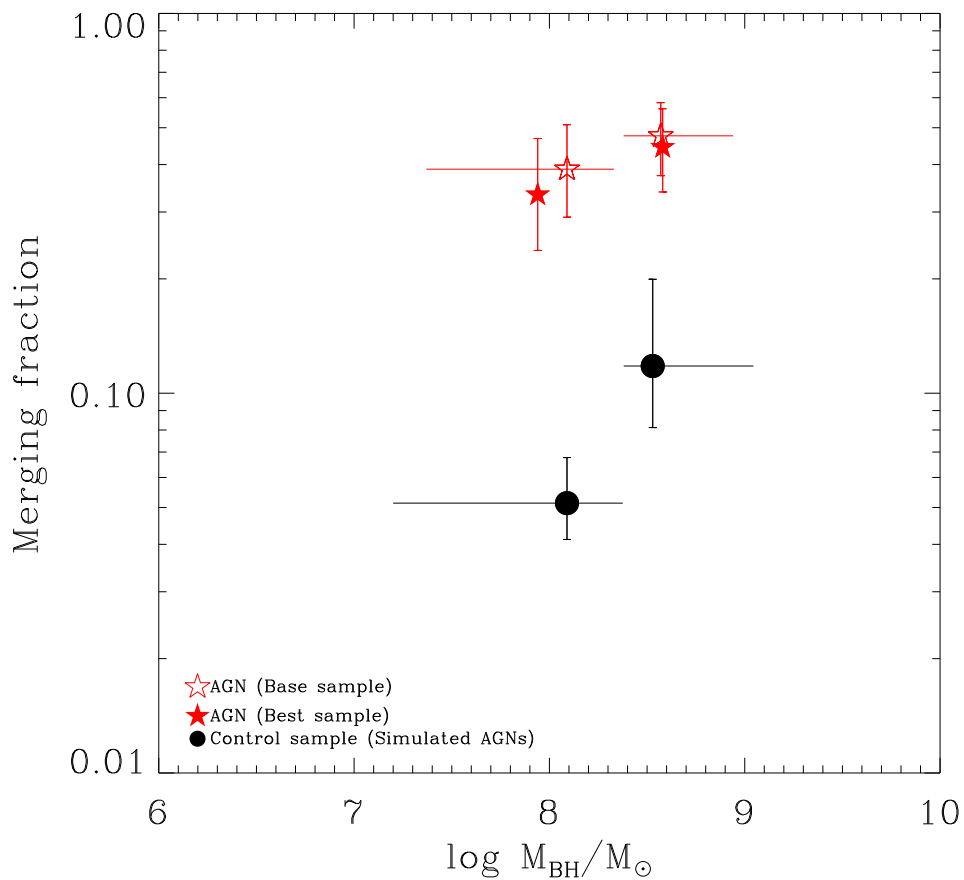


Fig. 18.— Merging fraction of AGNs and simulated AGNs (control sample) versus the black hole mass of the host galaxy. The merging fraction of simulated AGNs has been corrected for the difference in the  $M_{\text{BH}}$  distribution between the AGN and the control samples. The red stars are for AGNs in the base sample, and the filled red stars are for AGNs in the best sample ( $M_{\text{Nuc}}(R) < -22.44$ ). The filled black circles are for simulated AGNs.



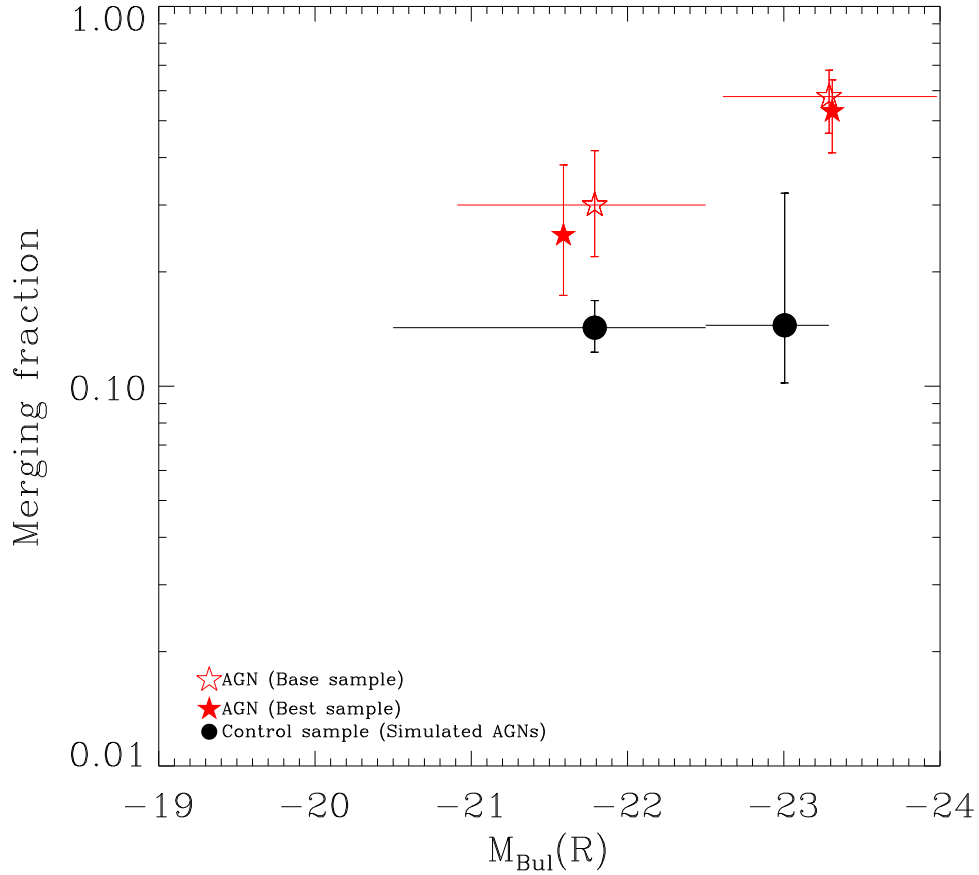


Fig. 19.— Merging fraction of AGNs and simulated AGNs (control sample) versus the bulge magnitude of the host galaxy. The merging fraction of simulated AGNs has been corrected for the difference in the  $M_R$  distribution between the AGN and the control samples. The red stars are for AGNs in the base sample, the filled red stars are for AGNs in the best sample ( $M_{\text{Nuc}}(R) < -22.44$ ), and the filled black circles are for simulated AGNs.